NASA TECHNICAL MEMORANDUM

NASA TM-88490

VORTEX SYSTEMS ON SLENDER ROTATING BODIES AND THEIR EFFECT ON THE AERODYNAMIC COEFFICIENTS

M. Fiechter

Translation of "Uber Wirbelsysteme an schlanken Rotationskörpern und ihren Einfluss auf die aerodynamischen Beiwerte," Deutsch-Französisches Forschungsinstitut (German-French Research Institute), Report No. ISL-10/66, December 14, 1966, Saint-Louis, France, pp. 1-54 (68N29391).

NATIONAL AERONATICS AND SPACE ADMINISTRATION
WASHINGTON, DC 20546 DECEMBER 1986

STANDARD TITLE PAGE

1. Report No.	2. Government Accession No.	3. Recipient's Catalog No.
NASA TM-88490		

4. Title and Subtitle	5. Report Date
VORTEX SYSTEMS ON SLENDER ROTATING BODIES AND THEIR EFFECT ON THE AERODYNAMIC COEFFICIENTS	December 1986
	6. Performing Organization Code
7. Author(s)	8. Performing Organization Report No.
M. Fiechter	10. Work Unit No.
	11. Contract or Grant No. NASW-4006
9. Performing Organization Name and Address	13. Type of Report and Period Covered
The Corporate Word, inc. 1102 Arrott Bldg. Pittsburgh, PA 15222	Translation
12. Sponsoring Agency Name and Address	14. Sponsoring Agency Code
National Aeronautics and Space Administration Washington, DC 20546	

15. Supplementary Notes: Translation of "Uber Wirbelsysteme an schlanken Rotationskorpern und ihren Einfluss auf die aerodynamischen Beiwerte," Deutsch-Franzosisches Forschungsinstitut (German-French Research Institute), Report No. ISL-10/66, December 14, 1966, Saint-Louis, France, pp. 1-54 (68N29391).

16. Abstract: The turbulent flow of rotational bodies up to a length of 20 diameters with various head shapes and cylindrical tails was examined in the subsonic wind tunnel of the ISL with the Mach number of M = 0.1. At angles of incidence lower than 30 degrees, a pair of symmetrical eddies rests stationary from head to tail on the trailing side, very close to the body. At angles between 30 and 60 degrees, the stationary eddies are asymmetrically pushed off. Between 60 and 90 degrees, the eddies detach themselves in an instationary manner. This includes, for example, the turbulent flow at the start-up of flying bodies in the presence of lateral winds. The results of measurements obtained by MELLO at M = 2, an impulse method, and the cross flow theory according to ALLEN are used for the comparison.

17. Key Words (Selected by Author(s))	18. Distribution Statement
	Unlimited

19. Security Classif. (of this report)	20. Security Classif. (of this page)	21. No. of Pages	22. Price
Unclassified	Unclassified	50	

NASA-HQ

Table of Contents

VORTEX SYSTEMS ON SLENDER ROTATING BODIES AND THEIR EFFECT ON THE AERODYNAMIC COEFFICIENTS

M. Fiechter

Introduction

At already minor disturbances in flight, slender rotational bodies can attain such large amplitudes in the swing of pendulum that the influences of inertia and tenacity of the air, circulating around the body, can no longer be neglected. In the process, the currents detach themselves from the body. At the trailing side, eddies form which allow the subpressure and also the cross currents to become substantially larger than what the potential theory calculations show, that is, the effects of tenacity are not given consideration. /7*

Experimental examinations at angles of incidence up to 90° and at stationary, incident flow, show various eddy systems. These were examined in the 1.2 m subsonic wind tunnel of the ISL (Fig. 1) at a flow velocity of V_0=34.2 m/s, corresponding to a Reynolds number of 110,000 in relation to the cylinder diameter.

The circular-cylindrical test bodies with various head shapes are shown in Fig. 2. Their total length amounted to 11.7, 16.3, and 20.9 cylinder diameters. The profile of the ogivalic head shape with the head length of $L_K=3D_0$ corresponds to that of the Standard Model AGARD - B with the local radius of

$$R=\frac{x}{3}\left[1-\frac{1}{9}\left(\frac{x}{D_0}\right)^2+\frac{1}{54}\left(\frac{x}{D_0}\right)^3\right] .$$

The cone-shaped head had an equal length of $L_K=3D_0$. The Body Series C consisted of straight-cut circular cylinders.

The directional-, pressure-, and velocity measurements in the area of eddies, the painted presentations of current lines close to the wall, the pressure distribution measurements at the surface, and the three-component measurements with built-in strain gauge scales in the wind tunnel, were augmented by photographs and films [1] of the eddy systems. These show the currents of the eddies in the water tunnel of the ISL

*Numbers in the margin indicate pagination in the foreign text.

(Fig. 3) [2] at a current velocity of 4 cm/s, corresponding to a Reynolds number of 400. /8

For angles of incidence up to 30°, a simple empirical relationship is given for the symmetrical eddy pair, for the location as well as for the circulation, and the beginning of the asymmetrical deflection of the eddies is defined as the symmetry boundary. The forces acting on the body are calculated with the help of an impulse method and the semi-empirical cross flow theory according to *Allen* [3]. Measurement results by *Mello* [5] at M=2 were used for comparison.

Nomenclature

c_M Coefficient of the tilting moment around the tail $M = c_M p_{do} S_Q L$, (negative at positive angles of incidence)

c_N Coefficient of the normal force $N=c_N p_{do} S_Q$

c_p Coefficient of pressure $(p-p_0)/P_{do} = (p-p_0)/Kp_0 M_0^2/2)$

c_T Coefficient of the tangential force $T=c_T p_{do} S_Q$

c_{WQ} Coefficient of the resistance of a laterally inflowing, infinitely large circular cylinder per diameter and unit of length $dW_Q=c_{WQ} p_{do} D\, dx$

d Core diameter of the eddy

D Body diameter at any given point x

D_0 Greatest body diameter = diameter of the cylinder

H Distance between center of pressure and tail

H_Q Distance between strongpoint of longitudinal cross-sectional area and the tail

L Maximum body length, reference length

L_K Head length

L_Z	Length of the cylindrical part	/9
M_0	Mach number of the undisturbed flow	
M_Q	Cross-current Mach number = $M_0 \sin$ å	
p	Local static pressure	
p_0	Static pressure of the undisturbed flow	
p_d	Dynamic pressure = $\rho V^2/2 = K p M^2/2$	
p_{do}	Dynamic pressure of the undisturbed flow	
r	Radial distance of a point normal to the body axis (x-axis), cylinder coordinate	
R	body radius at any given point x	
R_0	cylinder radius	
R	Reynolds number = $V_0 d_0/\nu$	
S	Cross-sectional area of body at any given point x	
S_0	Cross-sectional area of cylinder = maximum cross-sectional area	
S_Q	Longitudinal cross-sectional area of body through the x-axis, reference area = $\int_0^L D dx$	
V	Resultant velocity	
V_0	Velocity of undisturbed flow	
Vol.	Volume of the entire body = $\int_0^L (\pi D^2/4)\, dx$	
x y z	Coordinates in the body system, origin at the tip of the body	
å	Angle of incidence, angle between body axis and the direction of undisturbed flow	
η	Numerical ratio of the resistance of a laterally flowing, infinitely long circular cylinder to the resistance of an infinitely long circular cylinder	

θ Meridian angle of the rotational body, cylinder coordinate, = 0 on the inflowing side in the incident angle's plane /10

κ Isentropic exponent

ν Kinematic tenacity

ρ Density

Γ Strength of eddy, circulation $= \oint v_s \, ds$

Symmetrical, stationary adjoining pair of eddies

At angles of incidence å>5°, the currents detach themselves from the body, thus creating at the trailing side two eddies symmetrical to the plane of the angle of incidence and with an opposite direction of rotation. They move in spiral fashion and stationary along the body from tip to tail, only a small distance away from the surface. In Fig. 4, one can see the front eddy in the water current. The eddy current lines can be seen in terms of the thin threads made by a colored fluid exiting at a slight excess pressure from small drilled holes at the model's surface. These threads enclose the eddies in a spiral-like manner. In an air current, the pair of eddies moves in a similar way. The symmetry of the eddies is confirmed by the pressure distribution curves for å<30° in Fig. 14 and by the pictures of the currents close to the wall in Fig. 15 and 16.

The field of eddies of the body with L=16.3 D_0 total length and a cone-shaped head was examined in the wind tunnel at the cylindrical portion of the body with an ISL-vector probe [4], a hot wire anemometer, a filament anemometer, and a Pitot tube. These measurements show that up to å<30°, the eddies move in lines stationary along the body at velocities of $V_0 \cos å \; V_0$. Corresponding to the measuring results in Fig. 5, the radial distance r of the eddy centers from the body axis grows with

(1) $$r = (0.119 \pm 0.006) \times |å| + R_0$$

proportional to the distance from the tip of the body x and to the angle of incidence å. The eddies apparently have their origin in the normal plane x=o, one cylinder radius away from the tip of the body. The entered values for M=2 from [5] in this Fig. 5 calls attention to the fact that there is a similar interrelationship with r 0.15x |å| $+R_0$. /11

For all angles of incidence up to 30° and in all cross-sectional planes, the measurement points for all subsonic as well as supersonic velocities lie, according to [5], in about the same meridian planes which enclose an angle of about 46° between them (Fig. 6). The ratio of eddy distance y from the plane of the angle of incidence to the radial distance r is

$$y/r = \sin\Theta = 0.39 \pm 0.03 \approx \text{const.} \quad [2]$$

For the determination of the circulation, the median diameters of the eddy centers were measured with

$$d = (0.14 \pm 0.03) \times |å| \quad [3]$$

which increase similar to the radial distance r with the distance x from the tip of the body and the angle of incidence å.

In the cross-sectional planes, the eddy centers rotate normal to their axis with about constant angular velocity. According to presently available measurements, one can accept as median value of the peripheral velocity

$$V_0 \sin å \approx V_0 å \approx \text{const.} \quad [4]$$

at the boundaries of the eddy centers for all cross sections x and for all angles of incidence å, with a median error of about 20%. With this simplification, [3] and [4] become the circulation

$$|\Gamma| \approx d\pi V_0 |å| \approx 0.14\, \pi V_0 x å^2, \quad [5]$$

which as circulation coefficient per $\mathring{a}^2$: $|\Gamma| / (D_0 \pi V_0 \mathring{a}^2) = 0.14x/D_0$ in Fig.7 allows the detection of a relatively small deviation from the measuring points for M = 0.1. For M = 2, the coefficient becomes $|\Gamma| / (D_0 \pi V_0 \mathring{a}^2) \approx 0.25x/D_0$. /12

The sum of all normal forces dN/dx in the individual cross sections which are formed by the tenacity influences of the current up to location x on the body, is proportional to the impulse I_x of the eddies and their mirror eddies with circulation Γ_x in the cross-sectional plane at location x (see also *Bryson* [6] and *Mello* [5]).

With the identity $t = x/V_0 \cos \mathring{a} \approx x/V_0$ and from $dI/dt = dN/dx$, the impulse in cross section x

$$[6] \qquad I_x = \int_0^t \frac{dN_V}{dx} dt = \int_0^x \frac{dN_V}{dx} \frac{dx}{V_0} = \frac{N_V}{V_0} = \rho \Gamma_x^2 (y - y_i)$$

becomes equal to the impulse of the eddies in cross section x. According to the law of reciprocal radii: $r_i/R_0 = R_0/r$ (Fig. 9B), [2] becomes the difference of distances $y-y_i = 0.39\, R_0 (r/R_0 - R_0/r)$ and thus from [6] for x=L, the entire normal force becomes

$$[7] \qquad N_V = 0.109 \pi D_0 p_{d0} L \mathring{a} |\mathring{a}| (r/R_0 - R_0/r)$$

By using [1], one can see that $N_V \sim x^2 \mathring{a}^3 + x \mathring{a} |\mathring{a}| - \ldots$. If to these tenacity forces N_V the potential forces N_P are added at the head of the body, then the normal force coefficient

$$[8] \qquad c_N = c_{NP} + c_{NV} = (S_0/S_Q)\, 2\mathring{a} + N_V/S_Q\, p_{d0}$$

follows with $S_0 = \pi D_0^2/4$ and S_Q, the longitudinal cross-sectional area. In Fig. 8, the c_N-curve, calculated according to [8] for the body having a total length of $L = 16.3\, D_0$ and the cone-shaped head, was plotted against the angle of incidence. The curve agrees well with the measuring points of the force readings for the body with the cone-shaped and the ogivalic head. /13

The curve according to [16] with $c_{NV} = \eta\, c_{WQ} \sqrt{|\alpha|}$ gives somewhat larger values. The measured values according to [5] for M=2 gives almost double the amounts, since the circulation (see above) of the eddies and also the pressure on the inflowing side is greater than in the subsonic region.

Symmetry Boundaries

With larger angles of incidence and increased body lengths, the eddy pair becomes asymmetrical and one of the two eddies is eventually pushed away from the body. Both eddies retain their stationary character, as can be seen in water currents in Fig. 10. As soon as the eddies have reached the radial distance

$$r \approx 2R_0 = r_G , \tag{9}$$

then one can notice pronounced asymmetrical behavior in the measurements of the eddy centers at all angles of incidence. From [9] together with [1], one obtains

$$\sqrt{|\alpha|}\, x_G \approx 8.4\, R_0 \tag{10}$$

in rough approximation the symmetry boundaries for the eddy movement.

Below the boundary curve according to [10] in Fig.11, the eddies are symmetrical, and above it they are asymmetrical. Up to the symmetry boundary, the center diameters

$$d_G \approx R_0 \tag{11}$$

do not become greater than, say, the body radius. One of the two eddies is then more strongly shaped into an oval than the other.

Aside from that, the eddies at the symmetry boundary on their way in the meridian planes reach the curve

$$r - r_i = r - R_0^2/r = 2r \sin\theta = 2y, \tag{12}$$

which is entered as a dashed curve in Fig. 9B. This curve shows, according /14
to *FÖPPL* [7] (see also [6], [8], [9]), the stable locations of the symmetrical eddy pair behind laterally inflowing currents to the circular cylinders in potential currents. Along with [9] one obtains at the symmetry boundary from [12]

$$\sin\theta = 0.375 = \sin 22^\circ \qquad [13]$$

about the same coordinate as the one from measurements in [2] : 23° which roughly confirms the geometrical requirements of the symmetry boundary according to [10]. The physical requirements, which lead to the introduction of the deflection process, are similar to the requirements which are described by *LUDWIEG* [10] and *HUMMEL* [11] for the bursting process of tenacious eddy centers over delta wings. For rotational bodies, however, these eddies are closer to the body surface and closer to one another.

Asymmetrical Deflection of Stationary Eddies.

Up to the symmetry boundary, the distance of the eddies from the surface of the body is small enough so that the rotational energy of the eddies still succeeds in guiding the outer currents around the eddies. Beyond the symmetry boundary with $|\mathring{a}|\ x > 8R_0$ (Equation [10]), the distance of the eddies becomes so great, however, that the outer currents penetrate into the space between eddy and body surface, thus deflecting the eddy from the body. The fanned color threads in Fig. 10 clearly show this process. The deflected eddy departs from the body with a pronounced change in direction. Under the deflected eddy, a little down-stream, a new eddy is formed. This eddy remains close to the body for a while and further downstream it, too, becomes deflected. With an increase in the angle of incidence, the point of deflection moves up-stream. In the spaces on the other side of the body, the other eddy is also deflected, and down-stream a new eddy is formed as can be seen in Fig. 12.

Pressure distribution at å = 50° in Fig. 14 and the interface picture in /15
Fig. 15 show these asymmetries. The large, bright spots mark the locations of deflection and renewed formation of eddies. In Fig. 16, the distances between left and right alternating locations of deflection become smaller with an increase in the angle of incidence.

Unlike on the delta wing, the eddies on the rotational body have the chance to escape sideways to the outside as soon as they get too much in each others' way. The deflected eddy system remains stationary up to an angle of incidence of about 60°. On the delta wing, depending on the wing span chord, the area down-stream from the shattered eddies becomes instationary at angles of incidence from 25° to 35°.

At a small interface disturbance, i.e. from a trip wire, the stationary eddies become asymmetrical without being deflected at already very small angles of incidence (å>8°). This causes stabilizing tail fins to rotate the flight body around its longitudinal axis, as was shown in the film [12].

These three-dimensional stationary eddy systems which develop and become deflected above and next to one another, are comparable to the two-dimensional instationary eddies which, alternating left and right, form and become deflected at the lateral inflow to the circular cylinders.

Instationary Eddy Separation

At angles of incidence of about 60°, the instationary separation begins (Fig. 13) and can be recognized by the separating rows of eddies as they leave the body in equal time intervals (*KÁRMÁN'S* eddy street). The pressure equalization beginning at the tail, causes the instationary separation area to spread toward the tip of the body with a further increasing angle of incidence until finally, at an angle of incidence of 90° (Fig. 17), the entire cylindrical part of the body is involved. /16

Only at the head, a stationary , asymmetrically deflected eddy pair is retained.

The subpressure peaks in the curves of pressure distribution in Fig.14 have disappeared since the too sluggishly registering instruments have only given time-related median values. The interface pictures in Fig. 15 and 16 at å = 70°, 80°, and 90° are correspondingly equally gray between the bright stripes at the separation lines of the interface.

Cross Flow Theory

The stationary eddy currents and -deflection up to an angle of incidence of 60° permit the pick-up of the cross currents nearly two-dimensionally in each plane normal to the body axis. Thus each given cross-sectional plane receives the same incoming cross current velocity $V_0 \sin å$. According to *ALLEN's* semi-empirical cross flow theory (cross flow theory [3], [13], [14]), the potential forces at the head of the body [15], [16], which change with $\sin 2å$, receive additional forces for the entire body. These grow with $\sin^2 å$ and correspond to the forces at the laterally inflowing currents to the circular cylinder with instationary eddy separation. The schematic distribution of normal forces over the axis of the body is presented in Fig. 18.

The integrated pressure distribution curves for each single cross section of the body (i.e. Fig.14) are delivered by the distribution of the normal force plotted over the body axis in Fig. 19 and 20.

According to the cross flow theory, the distribution of the normal force per unit of length is

$$dN/dx = (dS/dx)p_{do}\sin 2å + D\eta c_{WQ}p_{do} \sin å |å| \qquad (14)$$

The first term corresponds to the value from the liniarized potential theory with the cross-sectional area $S = \pi D^2/4$ for any given point of the body. dS/dx means that potential forces only there, where the cross

section of the body changes in the x-direction: for the examined bodies this happened only at the head. In the second term, the tenacity-dependent normal force changes with the local diameter D and with the impact pressure of the cross flow velocity $p_{d0}\sin\alpha\,|\alpha|$. /17

The resistance coefficient per diameter and unit of length c_{WQ} of a laterally inflowing current against an infinitely long circular cylinder is assumed as being constant for the entire body. It corresponds with good approximation to measurements according to *GOWEN* and *PERKINS* [17] for a cylinder of 60 diameters in length (Fig. 21). For M = 0.1, c_{WQ}=1.20. For other velocities, the cross-flow Mach number $M_0\sin\alpha$ and the cross-flow Reynolds number $R_0\sin\alpha$ must not be ignored.

Finitely long circular cylinders reduce their cross-flow resistance by equalization of pressure at the cylinder tails. At subcritical Reynolds- and Mach numbers, according to Fig. 22, the length influence factor

$$\eta = c_{N(\alpha=90°)}/c_{WQ} \approx 0{,}62 + 0{,}006\,L/D_0 \qquad (15)$$

for $L/D_0 > 5$

changes about proportionally to the cylinder length L and was determined from the ratio of the resistance of an infinitely long circular cylinder at cross flow $c_{N(\alpha=90°)}$ to that of the infinitely long circular cylinder c_{WQ} [3]. The measurements also show that a laterally inflowing current against a finitely long circular cylinder with a head has about the same resistance as a replacement cylinder of equal longitudinal cross-sectional area and equal total length.

The measured values showing the distribution of the normal force at the cone-shaped head, are shown in Fig. 23A for α = 30° and also for smaller angles of incidence, a little under the dashed line which was calculated according to Equation (14). For α = 50° in Fig. 23B and also for angles of incidence between 30° and 60°, the measured values at the head

coincide pretty well with the solid line according to Equation [14] with the factor $\eta = 1$. At the cylindrical part of the body, the measured values scatter around the solid lines with $\eta = 1$ at all angles of incidence up to 60°. This leads to the conclusion that the adjoining as well as the deflected stationary eddies induce normal forces which grow essentially proportional to the cross flow impact pressure and correspond to the normal forces at the infinitely long, laterally inflowing currents at the circular cylinder with instationary separation of the eddies ($\eta = 1$) /18

At the leading edge of the cylindrical part, the pressure distribution related to the cross flow impact pressure (Fig. 14) changes only very little over the whole field of angles of incidence and approximately corresponds to the pressure distribution at potential flow $c_p = 1 - 4\sin^2\theta$. At the trailing edge, the median value at instationary separation of eddies corresponds to the pressure coefficient $c_p/\sin^2\alpha \approx 0.8$.

At angles of incidence of between 60° and 90°, the measured values drop with an increase in the instationary separation of eddies to the calculated values with the factor η. Only at the head are the measured values at 90° in Fig. 23C a little larger in relation to the stationary eddies at the head.

When Equation [14] is integrated over the entire body length L, then one obtains the normal force coefficient

$$[16] \quad c_N = \frac{N}{p_{do} S_Q} = \frac{S_o}{S_Q} \sin 2\alpha + n c_{WQ} \sin\alpha|\alpha| ,$$

which is referenced here to the longitudinal cross-sectional area.

The moment coefficient with the tail of the body as point of reference

$$[17] \quad c_M = \frac{M}{p_{do} S_Q L} = \frac{Vol.}{S_Q L} \sin 2\alpha + \frac{H_Q}{L} n c_{WQ} \sin\alpha|\alpha|$$

was also referenced to the longitudinal cross-sectional area S_Q and to the total length of the body. /19

In the first term, the abbreviation "Vol." refers to the entire body volume, and in the second term, "H_Q" refers to the distance of the longitudinal cross-sectional area's strong point from the tail.

From c_M/c_N one obtains the distance of the center of pressure from the tail H/L. For $\alpha \rightarrow 0°$, the center of pressure moves, under neglect of the quadratic second terms from (16) and (17), into the volume strong point of the head $H_K/L = Vol./S_0L$.

With head length L_K the head shapes become

CONE	OGIVE	
L_K 2/3	L_K 7/15	Distance of center of pressure from the tip,
L_KD_0 /2	L_KD_0 2/3	Longitudinal cross-sectional area of head,
L_KS_0 /3	L_KS_0 8/15	Volume of head.

The values presented with the ogivalic head-forms for parabola profiles deviate from that for circular arc tangents by less than 1% when $L_K \geq 3D_0$.

At c_M/c_N for $\alpha = 90°$, the linear first terms disappear from Equations (16) and (17), and the center of pressure is located in the strong point of the longitudinal cross-sectional area H_Q/L.

The following figures show a summary of the results from 3-component measurements as well as the pressure distribution measurements for all examined bodies. With the exception of the tangential force measurements, they differ only very little from one another, since all values were referenced to the longitudinal cross-sectional area. The theoretical curves were only entered for bodies of a length of 16.3 diameters. As mentioned before for the normal force curves of pressure distribution in Fig. 23, it is also the case here that, for bodies with a cone-shaped head in Fig. 24, the measured values for angles of incidence up to 30° lie closer to the dashed lines, calculated with the factor η. Between 30° and 60° they lie a little above the solid line with /20

$\eta = 1$, and from 60° to 90° they again approach the values with factor η. The constant crossing from ogivalic head to the cylindrical part diminishes these differences in all sectors of angles of incidence (Fig. 25) (see also [14]). Since the straight-cut cylinders in Fig. 26 show the same results for all measured lengths as the cylinders with heads, one may conclude from this that the eddy formation starts in a similar way at all bodies. The plotted curves were taken from the calculations from the cylinder with the ogivalic head.

The coefficients of the tangential force c_T in Fig. 27, measured as a function of the angle of incidence, were also referenced to the longitudinal cross-sectional area. The steep rise in the curves up to an angle of incidence of about 20° is, on the one hand, due to the growing share of the pressure, meaning the form resistance of the head and, on the other hand, due to the increasing subpressure at the tail. The form resistance, here meaning the form tangential force, should decrease with the impact pressure of the velocity components in the direction of the body axis $(\rho/2)V_0^2\cos^2\alpha$:

$$[18] \quad c_T = c_{T0}\cos^2\alpha \quad ,$$

corresponding to the plotted dotted lines. For the bodies with the ogivalic head in Fig. 27A the measured values are up to 60% larger, with the cone-shaped head in Fig. 27B they are up to 40% larger, and with the straight-cut circular cylinder in Fig. 27C they are up to 80% larger than those according to [18]. Because of the strong holdover influence on the circular flow around the tail at large angles of incidence, the faulty measured curves were replaced by the assumed curves (dashes curves).

To assume the direction of the potential forces to be in the middle between the normal to the body axis and the normal to the wind direction, as reasoned by the theoretical considerations by *WARD*, doesn't seem to

be applicable here, since negative tangential forces, meaning the forces against the direction of flow, would be the result. For the same reason, tenacity forces as well as the potential forces were assumed as being perpendicular to the body axis in Equations [16] and [17]. /21

Closing Remarks

On the examined rotational bodies, a symmetrical eddy pair moves, at stationary incoming flow with subcritical Mach- and Reynolds numbers, stationary from head to tail along the trailing side of the body, as soon as the angle of incidence becomes greater than about 5°. Upon reaching the symmetry boundary which is dependent on the angle of incidence as well as the length of the body, the eddies become asymmetrical and are pushed off the body but at that, remain stationary up to angles of incidence of 60°. The symmetrically adjoining as well as the asymmetrically deflected stationary eddies induced normal forces which, according to *ALLEN*, depend on the impact pressure of the cross flow components, meaning increase with the square of the angle of incidence. By means of the measuring results, the dependency of the eddy impulses on the body was proven from the third power of the angle of incidence. The greater forces at the head were reproduced by the linearized potential theory.

With these experimental investigations, the intention was to describe the still relatively unknown flow behavior at slender rotation-symmetrical flight bodies at larger angles of incidence in order to better understand the still largely obscure stability- and steering problems [20], [21]. It is possible, for example, that slender flight bodies with stabilizing fins, on leaving the starting ramp, at a vertical take-off with ground wind, at the propellant cutoff of the rocket booster, at controlled turns etc., can experience angles of incidence which are substantially greater than 5°.

The similarity of eddy formation in slow water currents, /22
subsonic-, supersonic-, and also hypersonic currents (see i.e.[19]), is understandable because the interaction of pressure-, inertia-, and tenacity forces forms the flowing medium into eddies. Since eddies move in a stationary way along the incoming flow slanted toward the body, one is justified to look upon these eddies in the cross-sectional planes normal to the body axis as plane eddies. From this follows that the flow of eddies and their effect on the body itself and also on its controls depend on the impact pressure of the flow components lateral to the body axis $V_Q=V_0\sin\alpha$ or $M_Q=M_0\sin\alpha$ and on the Reynolds number $R_Q = R_0\sin\alpha$. The influence of compressibility, of the local pressure surges, of the impact wave on the eddies depends also on these conditions. *CURRY* and *REED*, for example, at hypersonic velocities noticed eddies which were asymmetrically deflected at minor disturbances. The lateral force which, therefore, is no longer located in the resultant angle of incidence plane, can increase the oscillating angle so much that the flight body axis cannot be returned into the flight track tangent. In addition, the asymmetrical field of eddies causes roll moments at the controls and possibly autorotation, as the film [12] shows it. These catastrophic flight situations (catastrophic yaw and roll-lock-in) cannot be explained, according to *NICOLAIDES* [23] and [22], by the the well-known coupling phenomena of rotation- and pendulum frequency, so that it is close at hand to see asymmetrical eddies as the cause for this.

REFERENCES

[1] M. FIECHTER
Stationäre und instationäre Wirbel an einem schlanken Rotationskörper mit ogivalem Kopf in Wasserströmung
(Stationary and instationary eddies on a slender rotational body with ogivalic head in water currents)
ISL Colortone Film (1966)

[2] H. WERLE
Aperçu sur les possibilités expérimentales du tunnel hydrodynamique à visualisation
ONERA NT 48 (1958)

[3] H. J. ALLEN
Estimation of the forces and moments acting on inclined bodies of revolution of high fineness ratio
NACA RM A 9126 (1949)

[4] R. RAMSHORN
Über ein zeitsparendes Verfahren zur Messung des Geschwindigkeitsvektors (About a time-saving method for measuring velocity vectors)
WGL-Bericht 5/1962, p. 189-195

[5] J. F. MELLO
Investigation of normal force distributions and wake vortex characteristics of bodies of revolution at supersonic speeds
J. aero. sci. 26 (1959) p. 155-168

[6] A. E. BRYSON
Symmetric vortex separation on circular cylinders and cones
J. Appl. Mech. (1959/12) p. 643-648

[7] L. FOPPL
Wirbelbewegung hinter einem Kreiszylinder (Eddy movement behind a circular cylinder)
Bayr. Akad. Wiss. (1913) p. 1-18

[8] J. N. NIELSEN
Missile aerodynamics
McGraw-Hill (1960) p. 91-94

[9] K. WIEGHARDT
Theoretische Strömungslehre (Theoretical study of currents)
Teubner (1964) p. 87-88

[10] H. LUDWIEG
Erklärung des Wirbelaufplatzens mithilfe der Stabilitätstheorie für Strömungen mit schraubenförmigen Stromlinien (Explanation of eddy burstings with the help of the stability theory for currents with spiral-shaped current lines)
Z. Flugwiss. 13 (1965) p. 437-442

[11] D. HUMMEL
Untersuchungen uber das Aufplatzen der Wirbel an schlanken Deltaflügeln (Investigations into the bursting of eddies on slender delta wings)
Z. Flugwiss. 13 (1965) p. 158-168

[12] M. FIECHTER
Autorotation schlanker Flugkörper mit vier Dreieckflossen
(Autorotation of slender flight bodies with four triangular fins)
ISL-Colortone Film (1966)

[13] H. J. ALLEN, E. W. PERKINS
A study of viscosity effects of flow over slender inclined bodies of revolution
NACA Rep. 1048 (1951

[14] E. W. PERKINS, L. H. JORGENSEN
Comparison of experimental and theoretical normal-force distributions including Reynolds number effects on an ogive-cylinder body at Mach number 1.98

[15] M. D. van DYKE
First and second order theory of supersonic flow past bodies of revolution
J. aero. sci. 18 (1951) p. 161-178

[16] H. R. VOELLMY
Experimentelle Untersuchungen an verschieden stark konvergenten, schlanken Rotationskörpern bei mässig hohen Überschallgeschwindigkeiten (Experimental investigations on various highly convergent, slender rotational bodies at moderately high supersonic speeds)
ETH - Zürich, Inst. f. Aerod. Mitt. No. 24 (1958)

[17] F. E. GOWEN, E. W. PERKINS
Drag of circular cylinders for a wide range of Reynolds numbers and Mach numbers
NACA TN 2960 (1953)

[18] G. N. WARD
Supersonic flow past slender pointed bodies
Qu. J. Mech. Appl. Math. vol. 2/1 (1949) p. 75-97

[19] F. MYSLIWETZ
Body lift and Newtonian theory
Z. Flugwiss. 11 (1963) p. 247-254

[20] M. FIECHTER
Experimentelle Untersuchungen der Rollstabilität von rotations-symmetrischen Flugkörpern mit kreuzweise angeordneten Deltaflügeln geringer Spannweite bei grossen Anstellwinkeln im Unterschallwind-kanal (Experimental investigations of roll stability of rotation-symmetrical flight bodies with traversely-mounted delta wings of limited wing-spread at large angles of incidence in the subsonic wind tunnel)
ISL-Report 12/63

[21] M. FIECHTER
Flugkörper mit vier Dreieckflossen ohne Rollmoment (Flight bodies with four triangular fins without roll moment)
Technical Bulletin ISL - T 28/64

[22] W. H. CURRY, J. F. REED
Measurement of Magnus effects on a sounding rocket model in a supersonic wind tunnel
AIAA Paper No. 66 - 754

[23] J. D. NICOLAIDES
A review of some recent progress in understanding catastrophic yaw
AGARD Rep. 551 (1966)

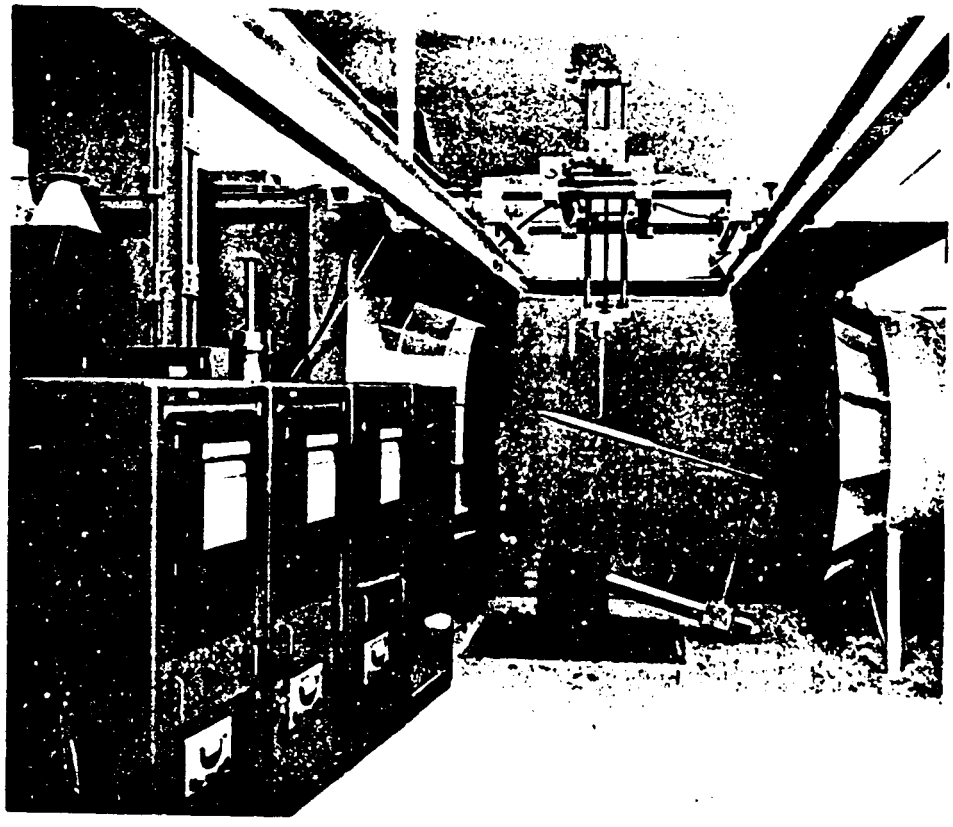

Fig. 1

Measuring track of the 1.2 m - wind tunnel (Type PRANDTL) with model body, vector probe on sliding device and plotting instruments

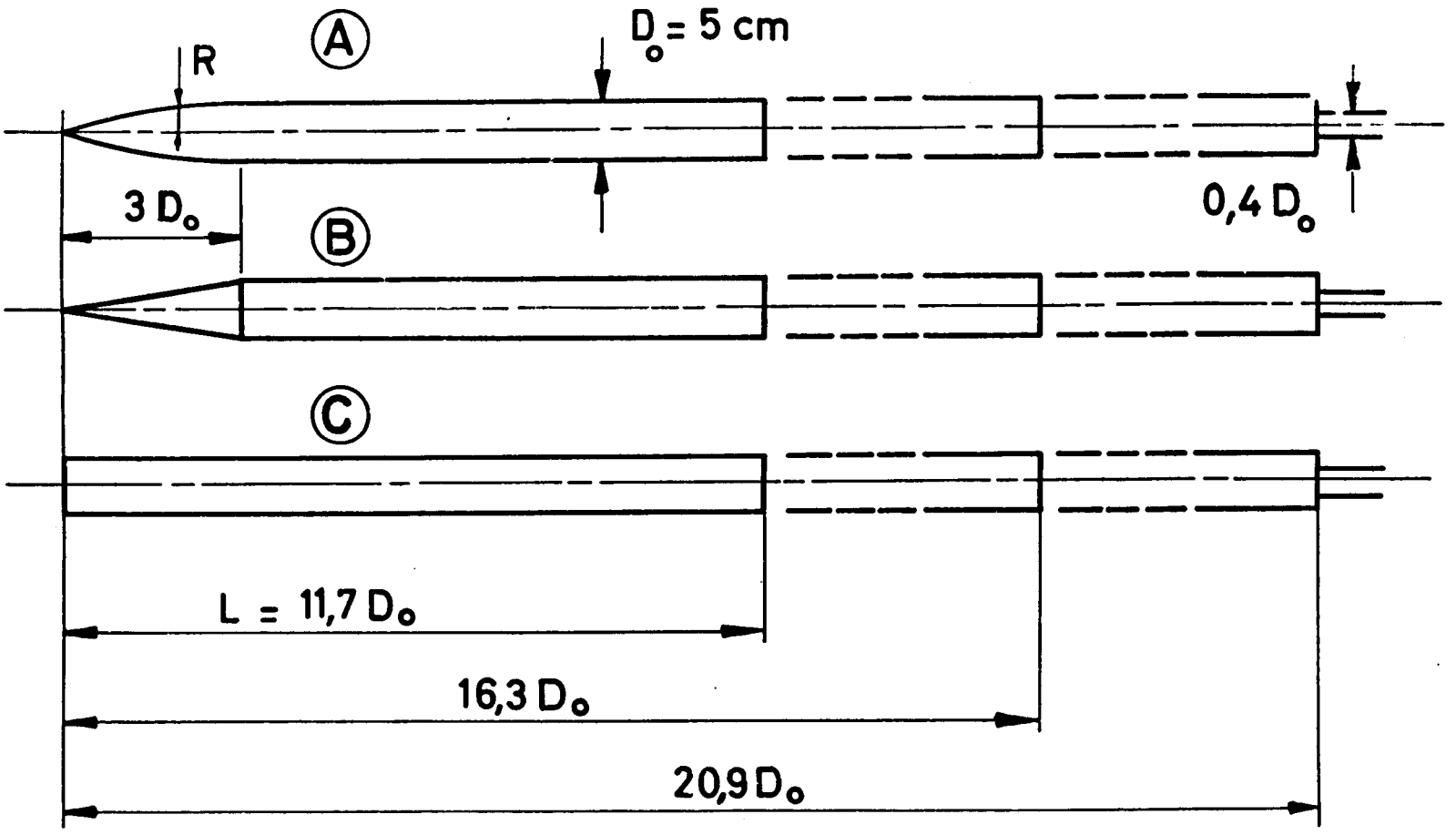

Fig. 2: Wind tunnel models

(A) Circular cylinder with ogivalic head,
(B) with cone-shaped head
(C) straight cut

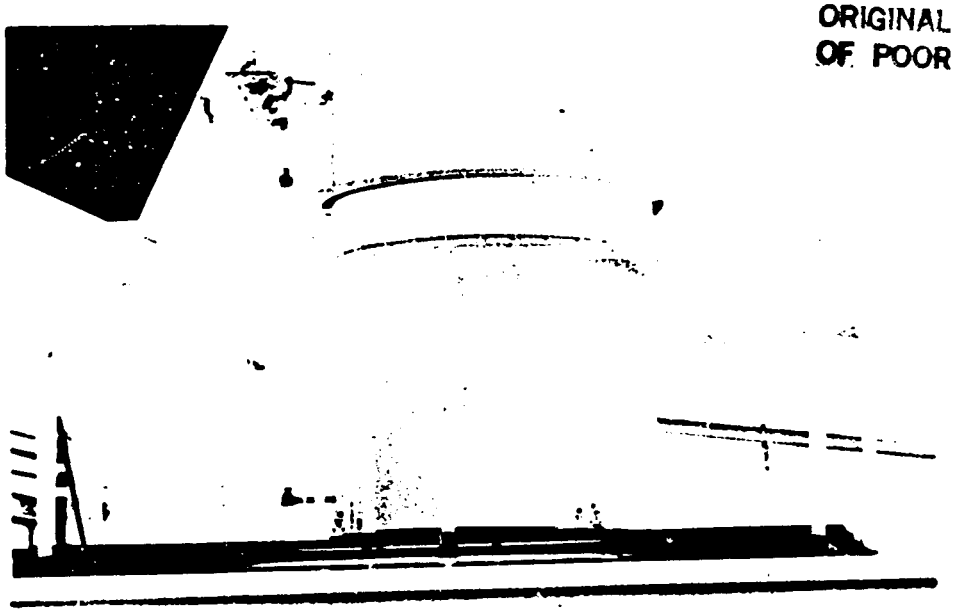

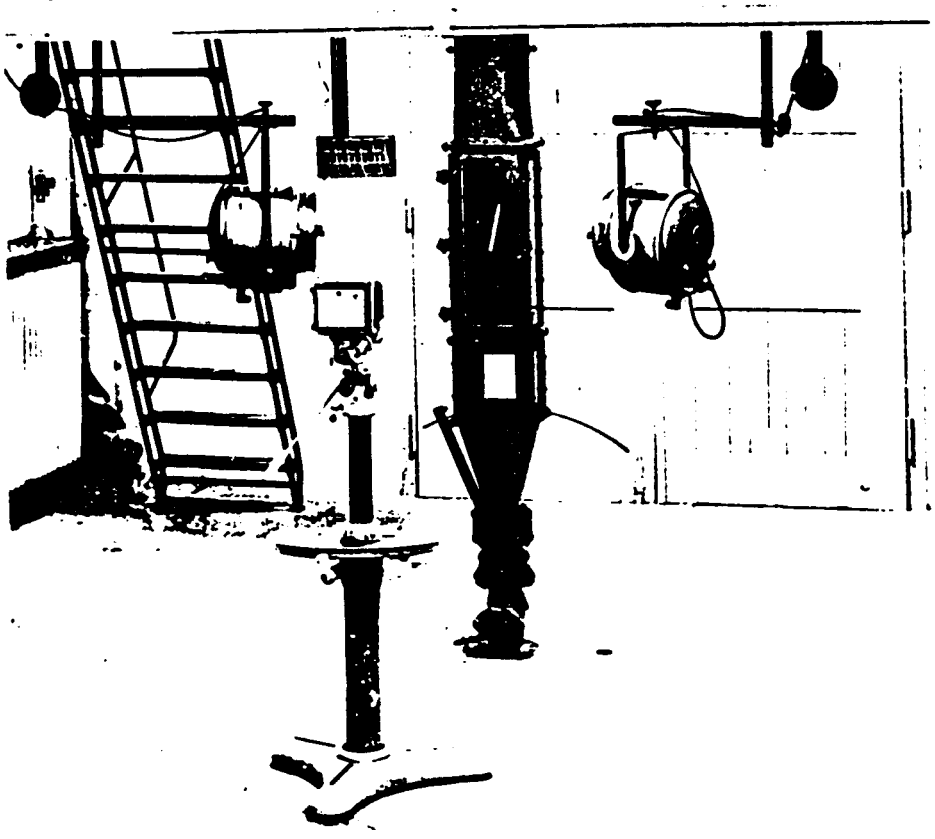

Fig. 3

Water channel
with gravity drive
(Type WERLE).

Cross section of measuring track 25 cm x 25 cm,
continuous current up to 10 cm/s velocity

Fig. 4

Eddy current lines in water channel, current from left to right, angle of incidence 25°

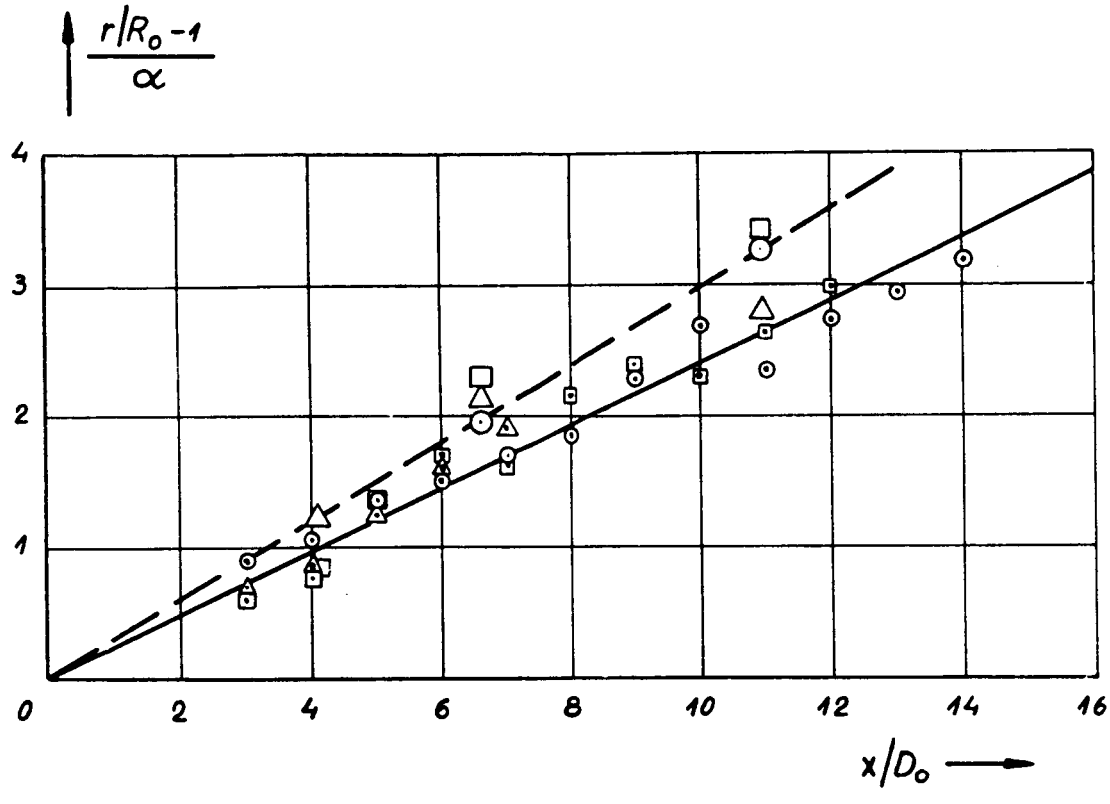

Fig. 5

Radial distance r of the eddy centers per angle of incidence å as a function of the distance from the body tip x according to Equation (1)

Angles of incidence 15° ⊙, 20° ⊡, 24° ▲ ISL M=0,1
16° ○, 20° □, 24° △ MELLO [5] M=2

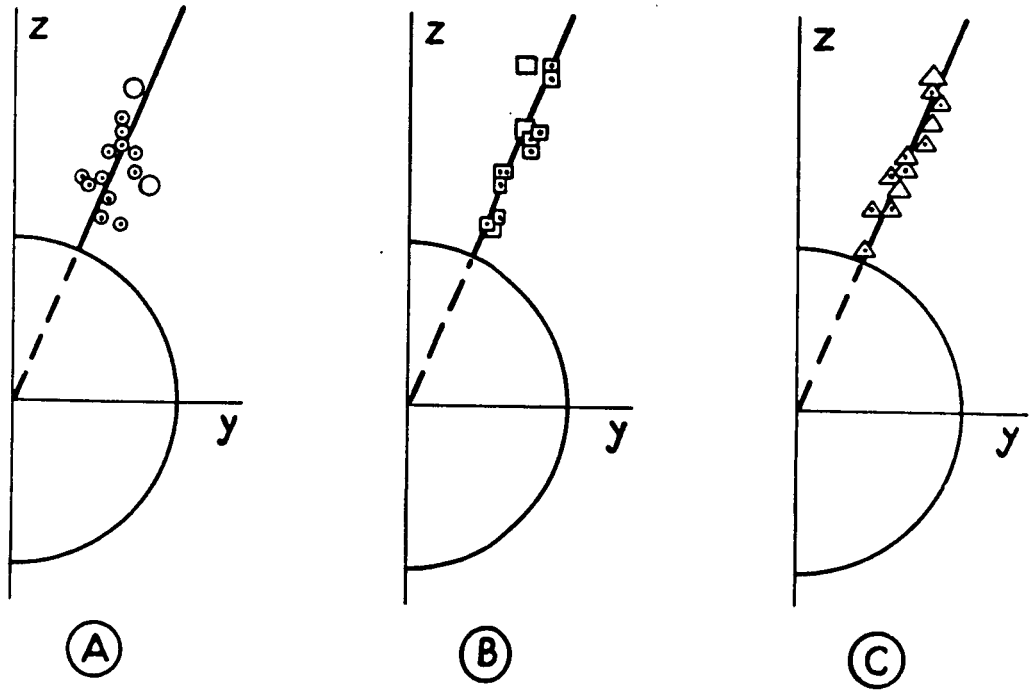

Fig. 6

Position of eddy centers in the various cross-sectional planes at angles of incidence 15° (A), 20° (B), 24° (C), symbols same as Fig. 5

_____ Meridian plane according to Equation (2)

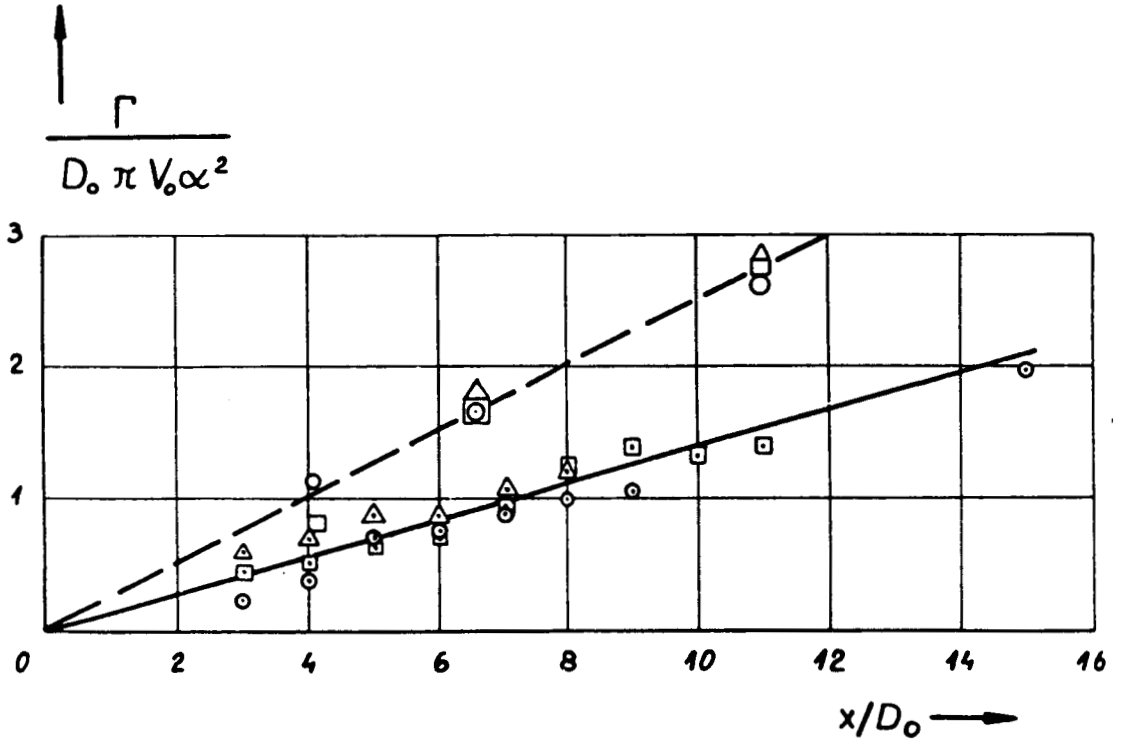

Fig. 7

Circulation coefficient per $\mathring{a}^2$ as a function of the distance x
from the body tip according to Equation (5)
Symbols same as in Fig. 5

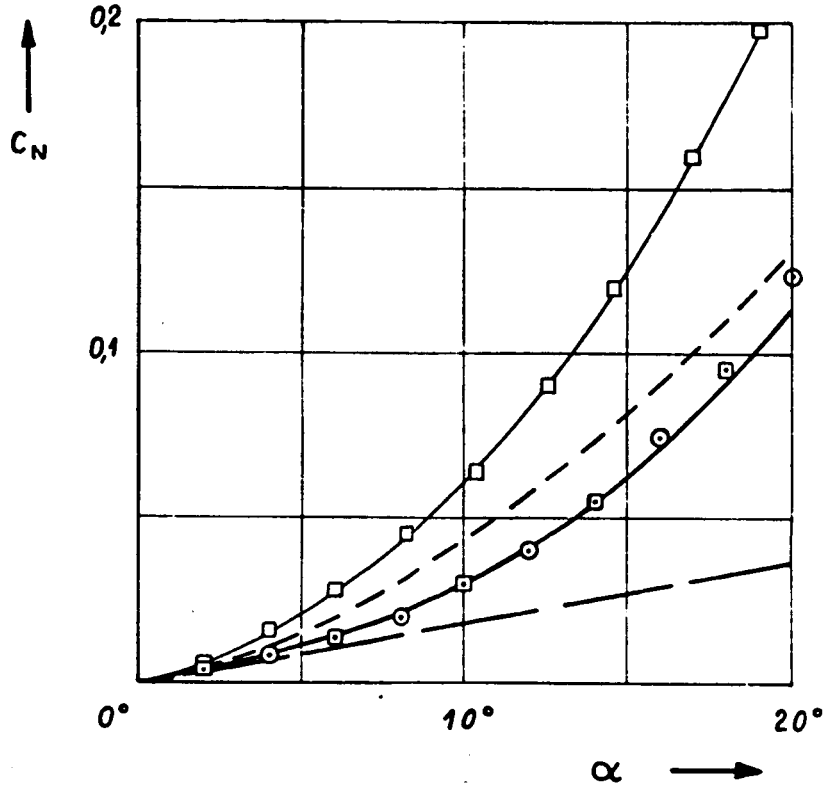

Fig. 8

Normal force coefficient as a function of the angle of incidence

——— Equation (8)

— — — Equation (16)

—— —— $c_{NP} = 2\mathring{a}S_0/S_Q$

⊙ L = 16.3 D_0 ogivalic head M = 0.1

⊡ L = 16.3 D_0 cone-shaped head M = 0.1

□ L = 13.2 D_0 cone-shaped head M = 2

acc. to [5]

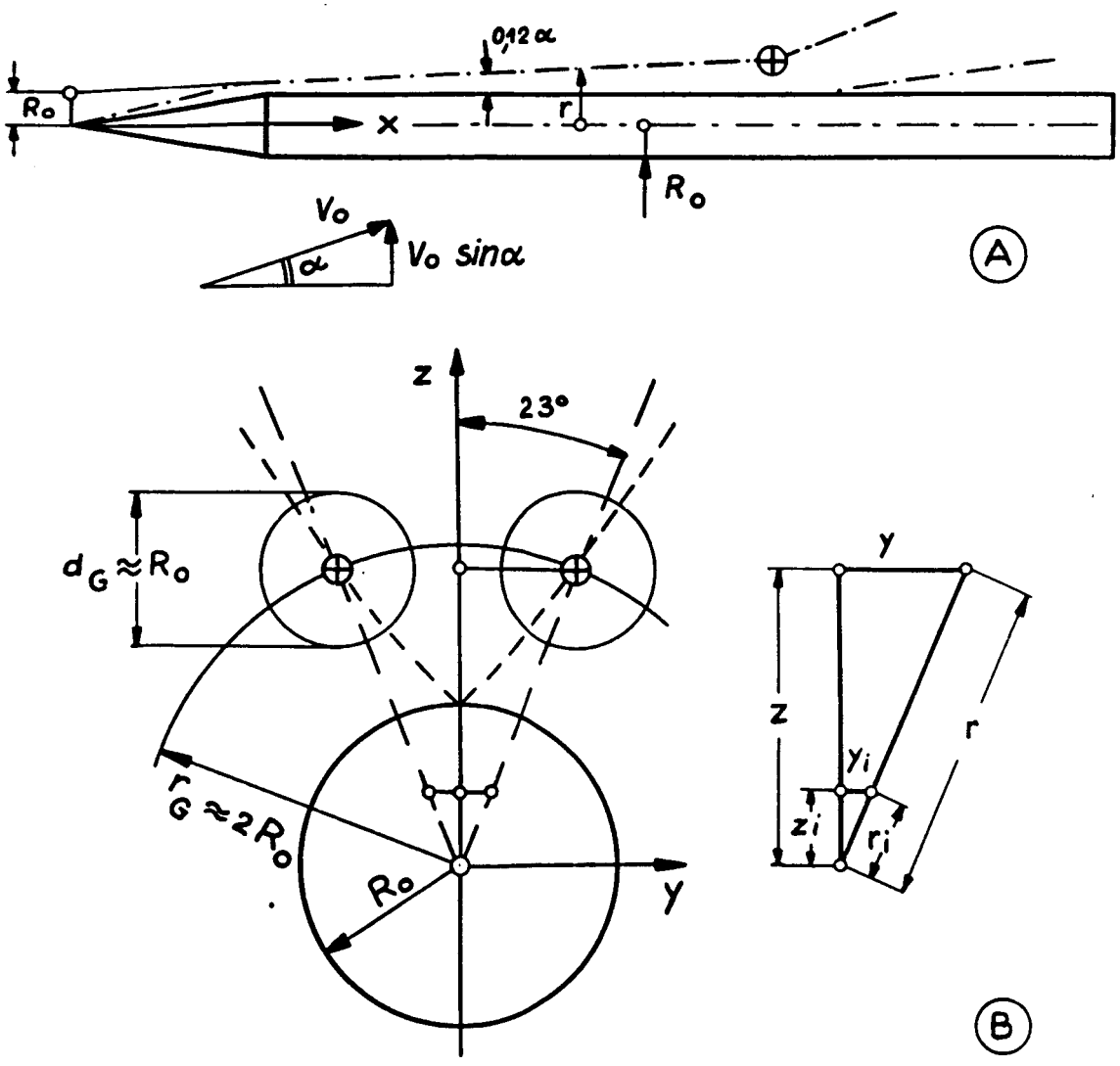

Fig. 9

Schematic representation of eddies

(A) sideview
(B) cross section at the symmetry boundary
– – – – – FÖPPL curve according to Equation (12)
—·—·— radial distance according to Equation (1)
— — — meridian planes according to Equation (2)
⊕ symmetry boundary according to Equation (10)

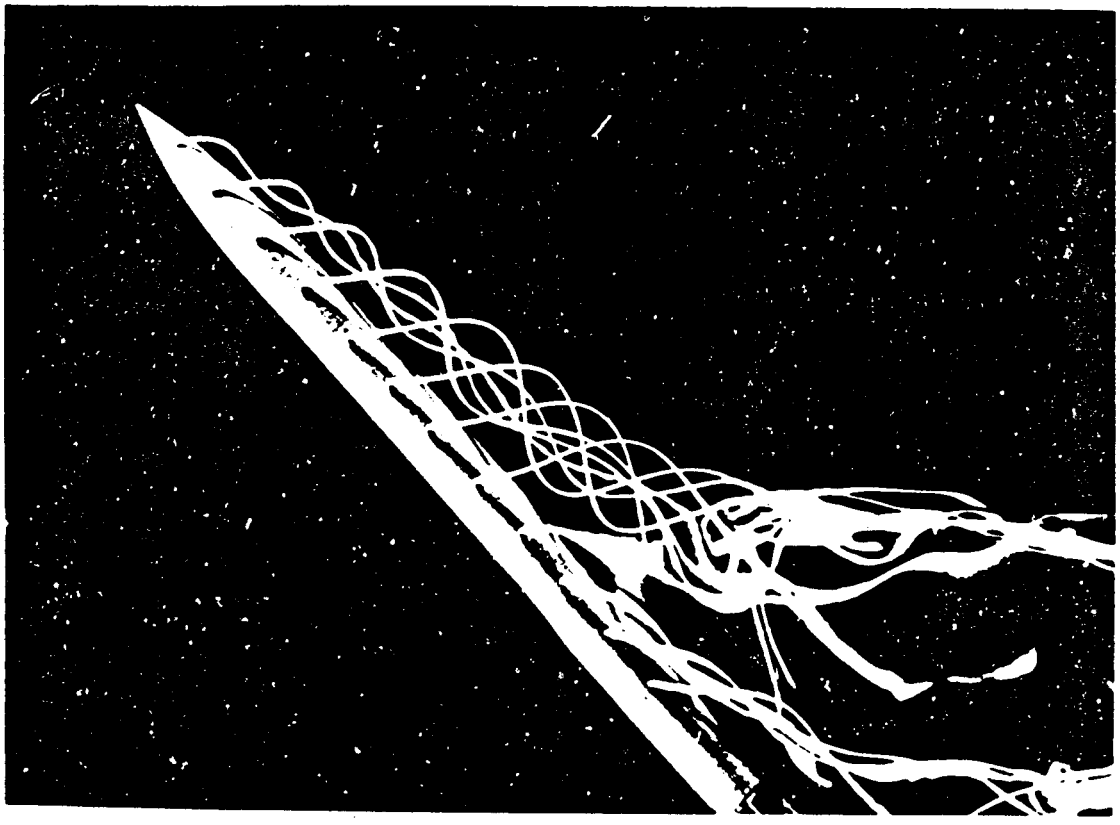

Fig. 10

Eddy deflection in water channel, angle of incidence 48°

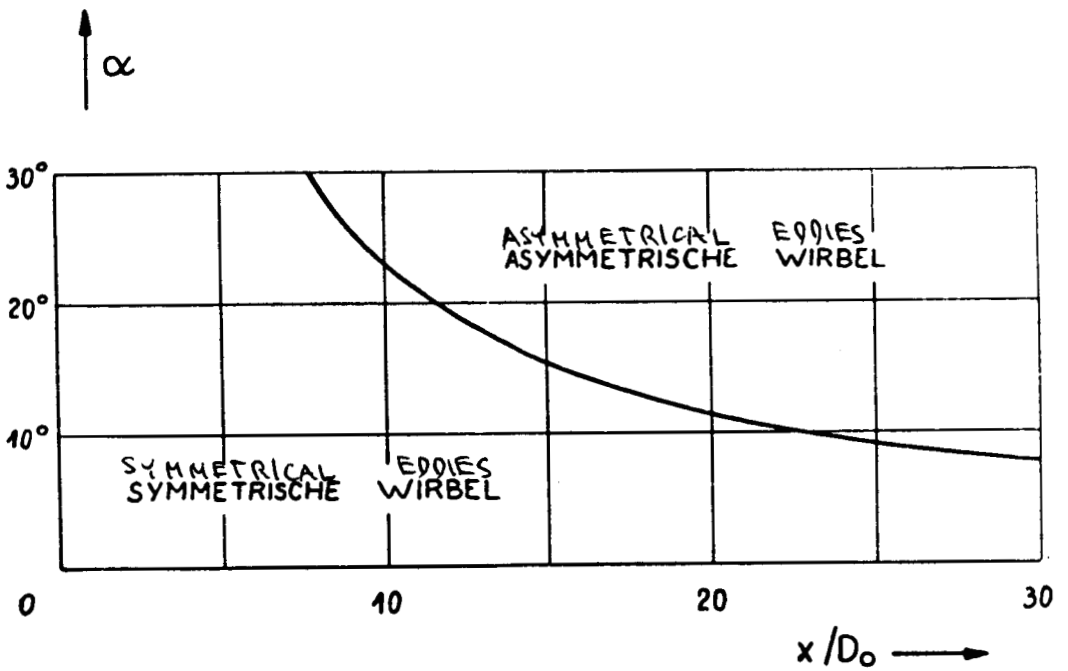

Fig. 11

Symmetry boundary according to Equation (10)

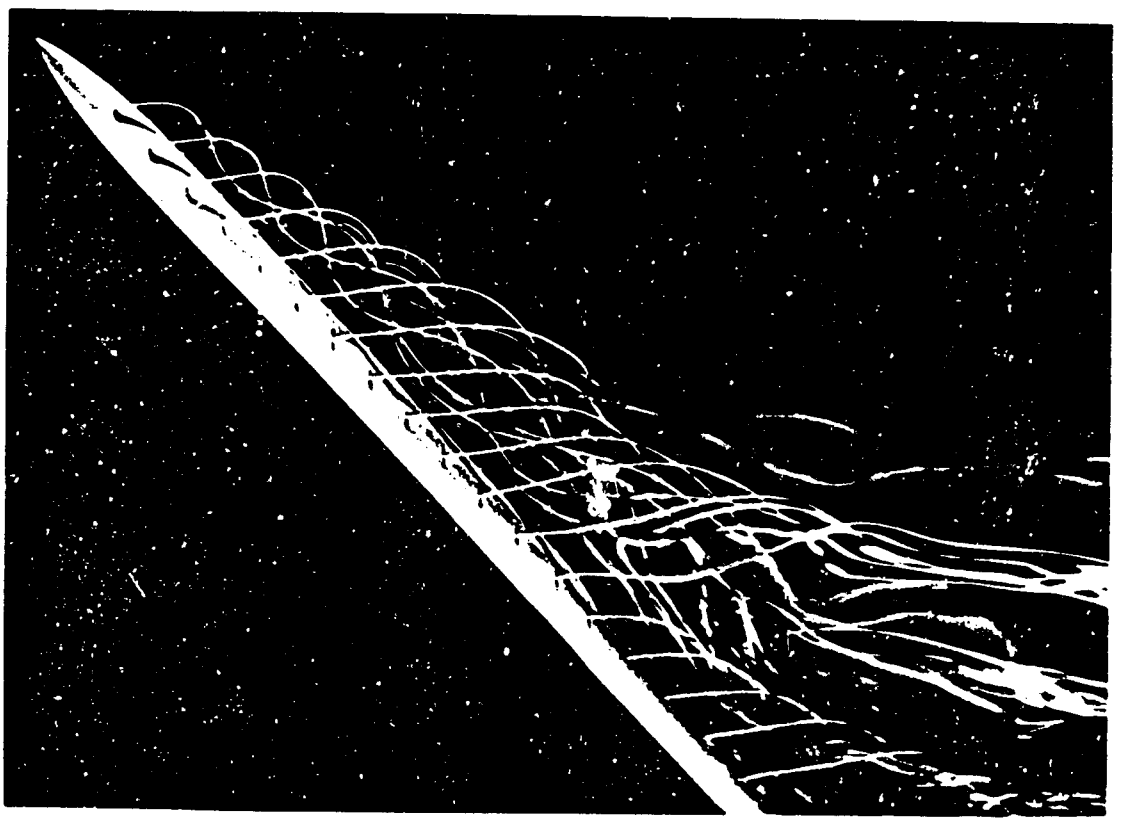

Fig. 12

Stationary, asymmetrical eddy systems in water channel
angle of incidence 48°

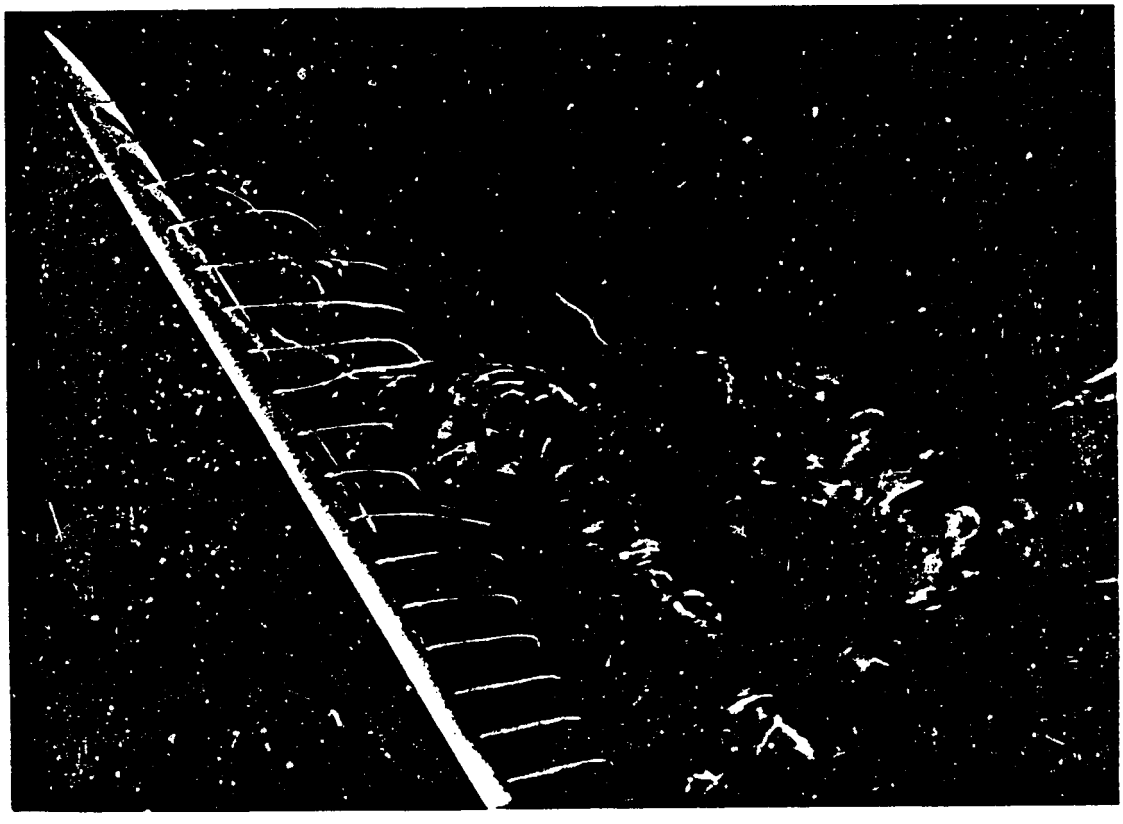

Fig. 13

Stationary and instationary eddies in water channel,
angle of incidence 60°

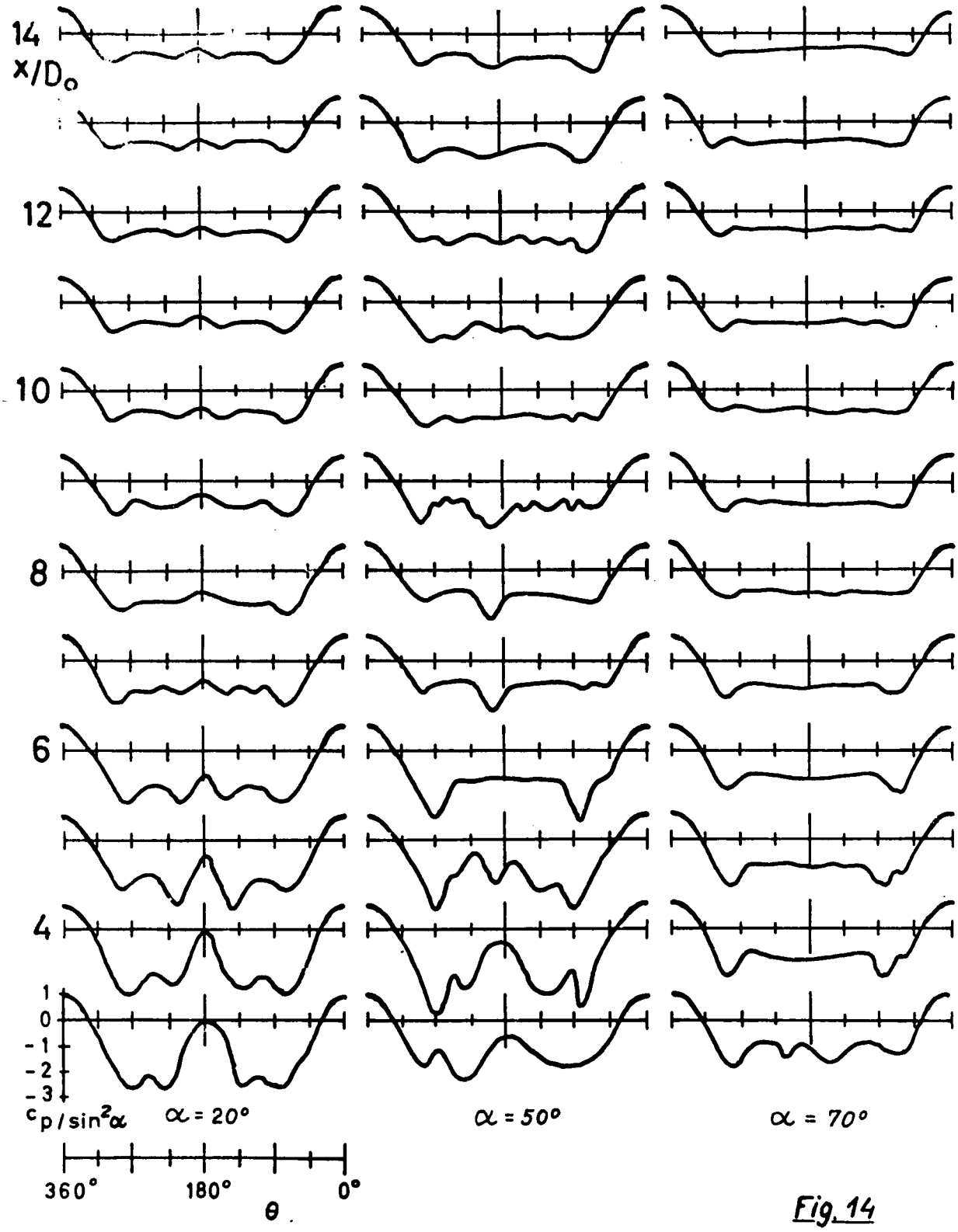

Fig. 14

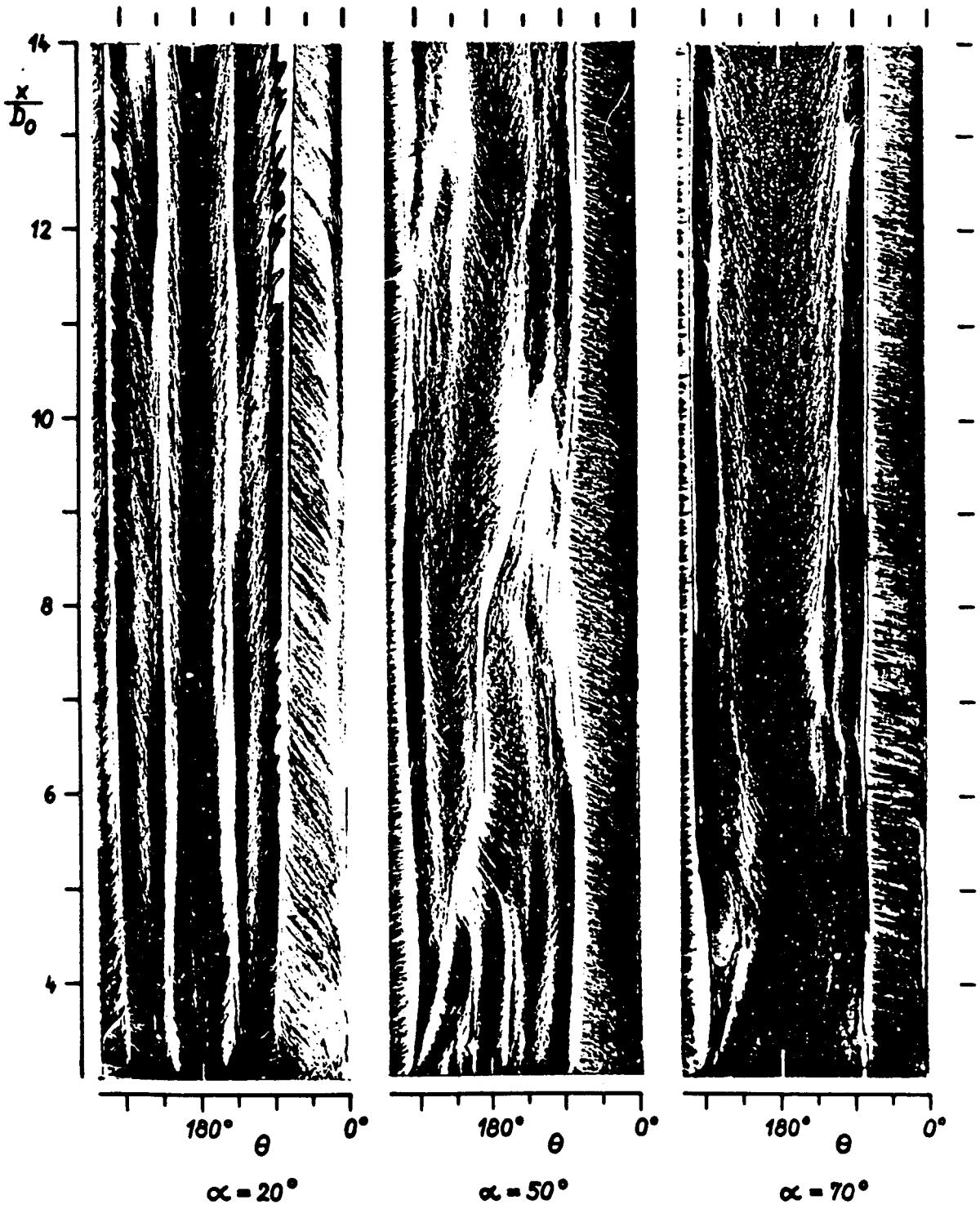

Fig. 15

Current lines close to wall at cylindrical part of body, like Fig. 14

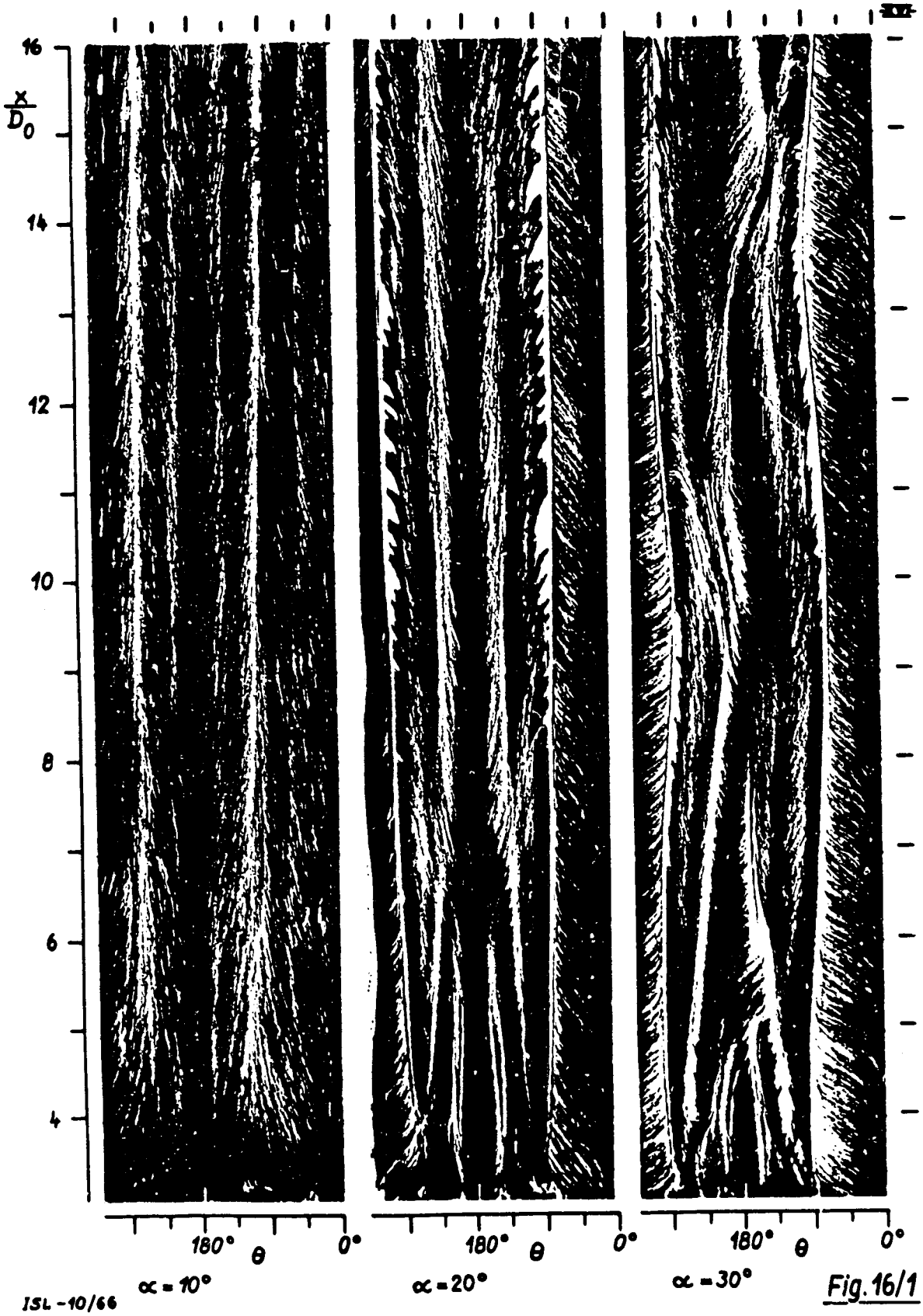

ISL-10/66

Fig. 16/1

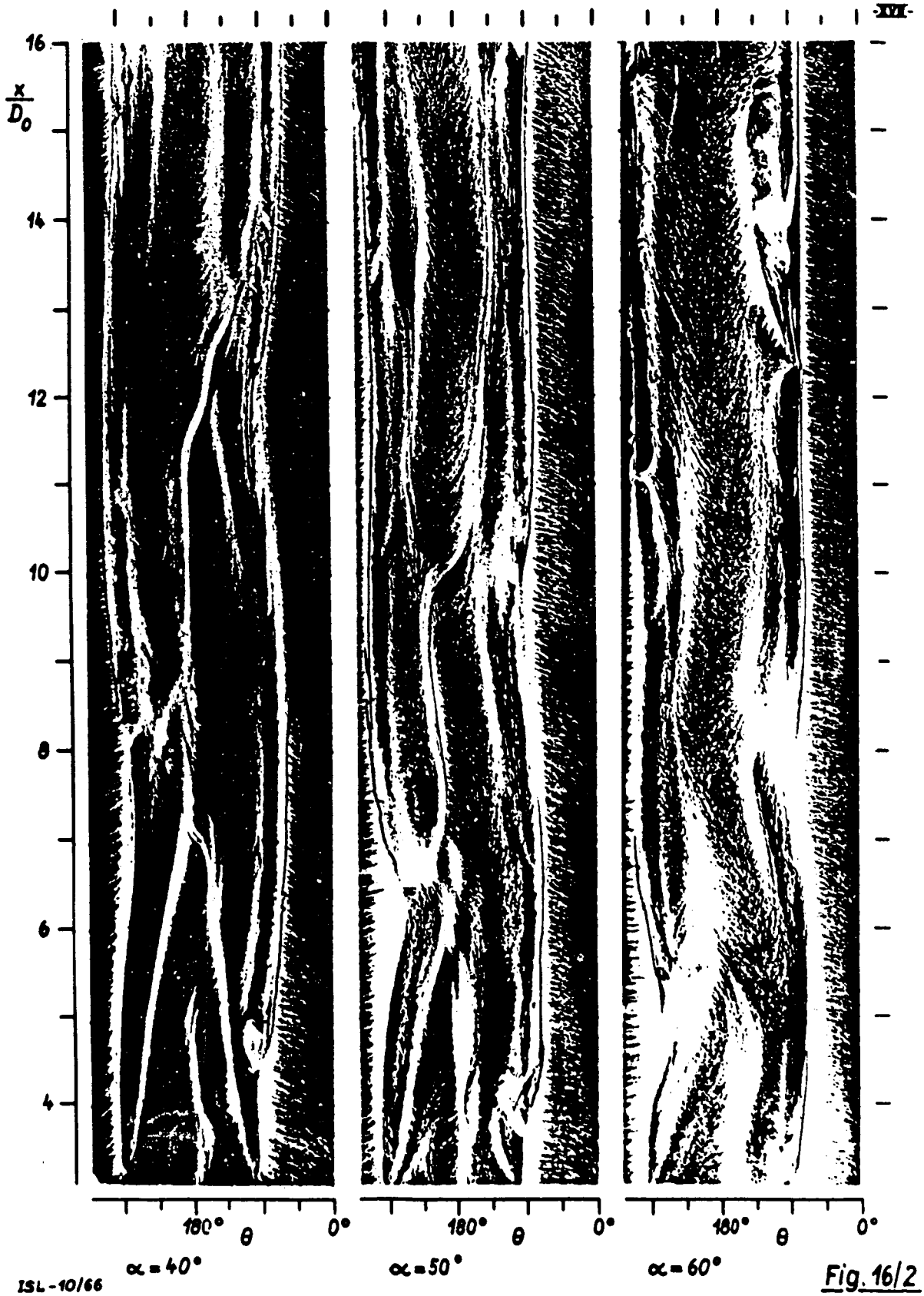

ISL-10/66

Fig. 16/2

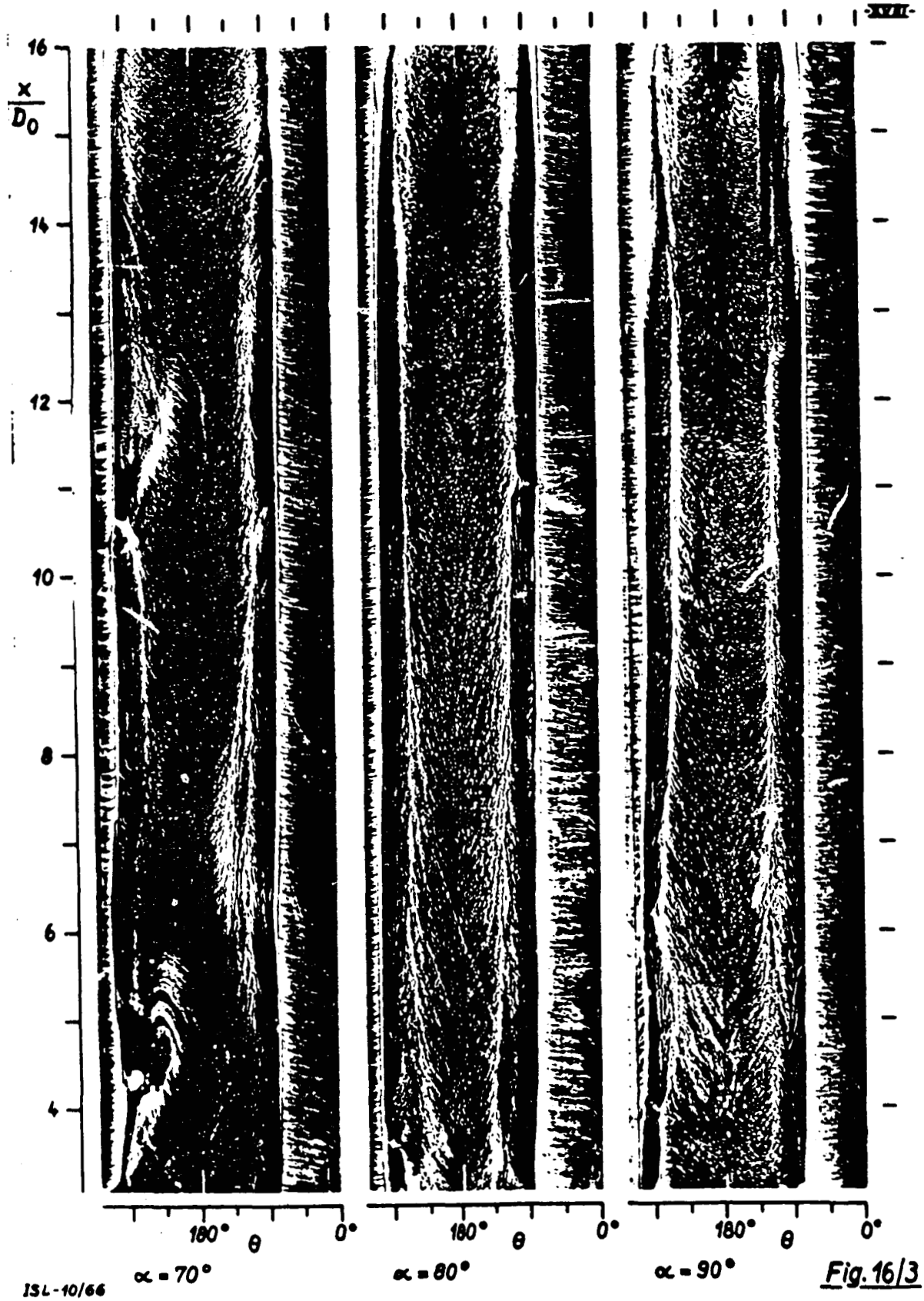

ISL-10/66

Fig. 16/3

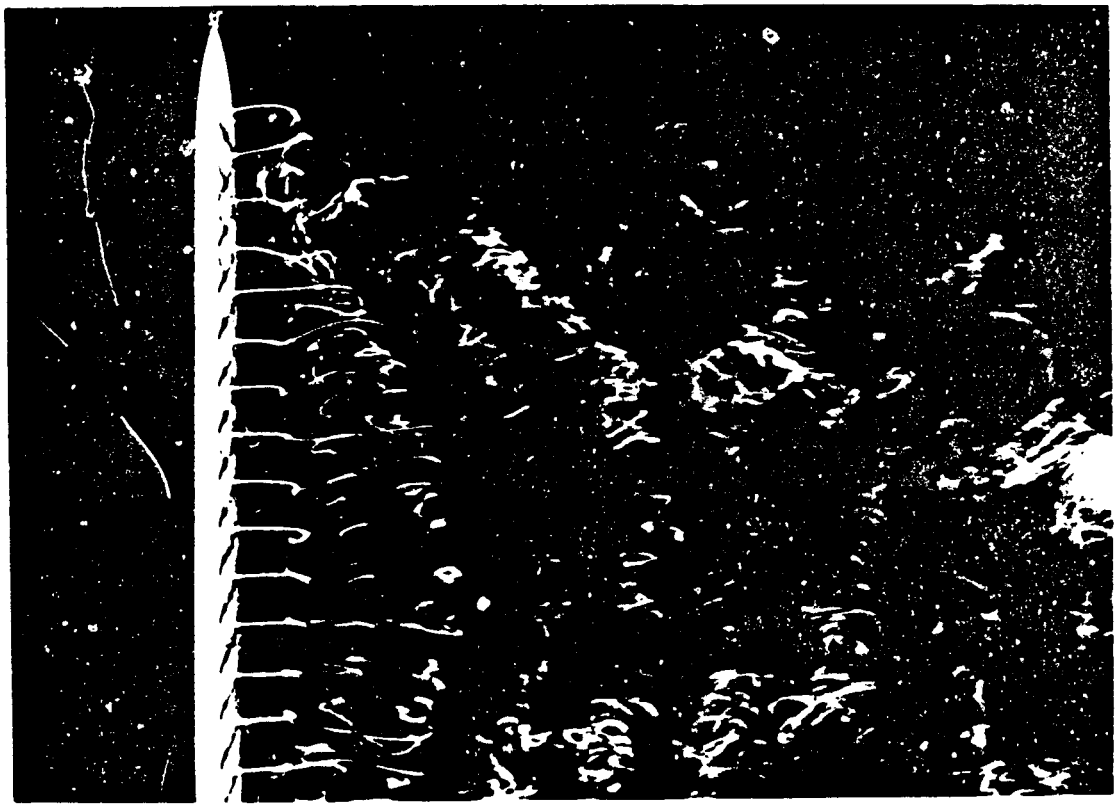

Fig. 17

Instationary eddies in water channel, angle of incidence 90°

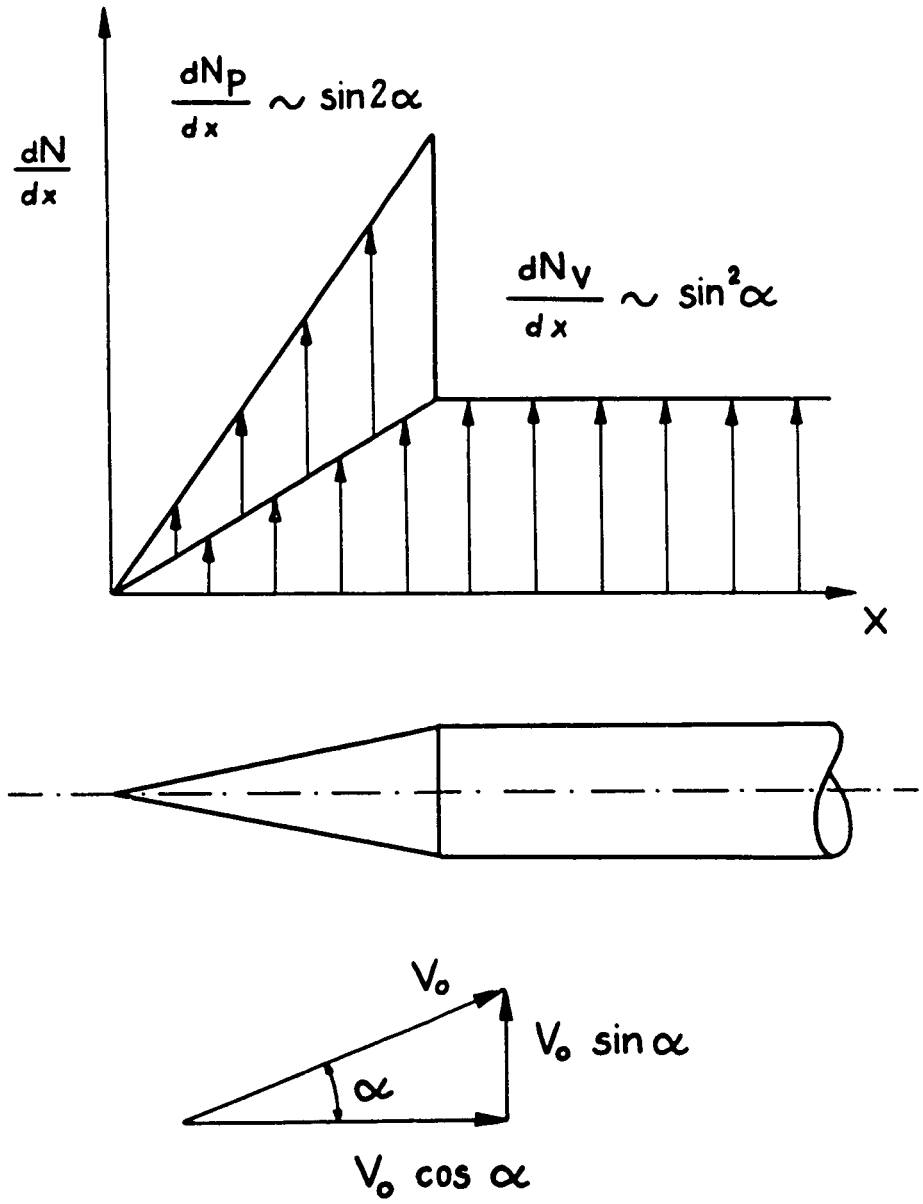

Fig. 18

Schematic representation of normal force distribution dN/dx above the body axis

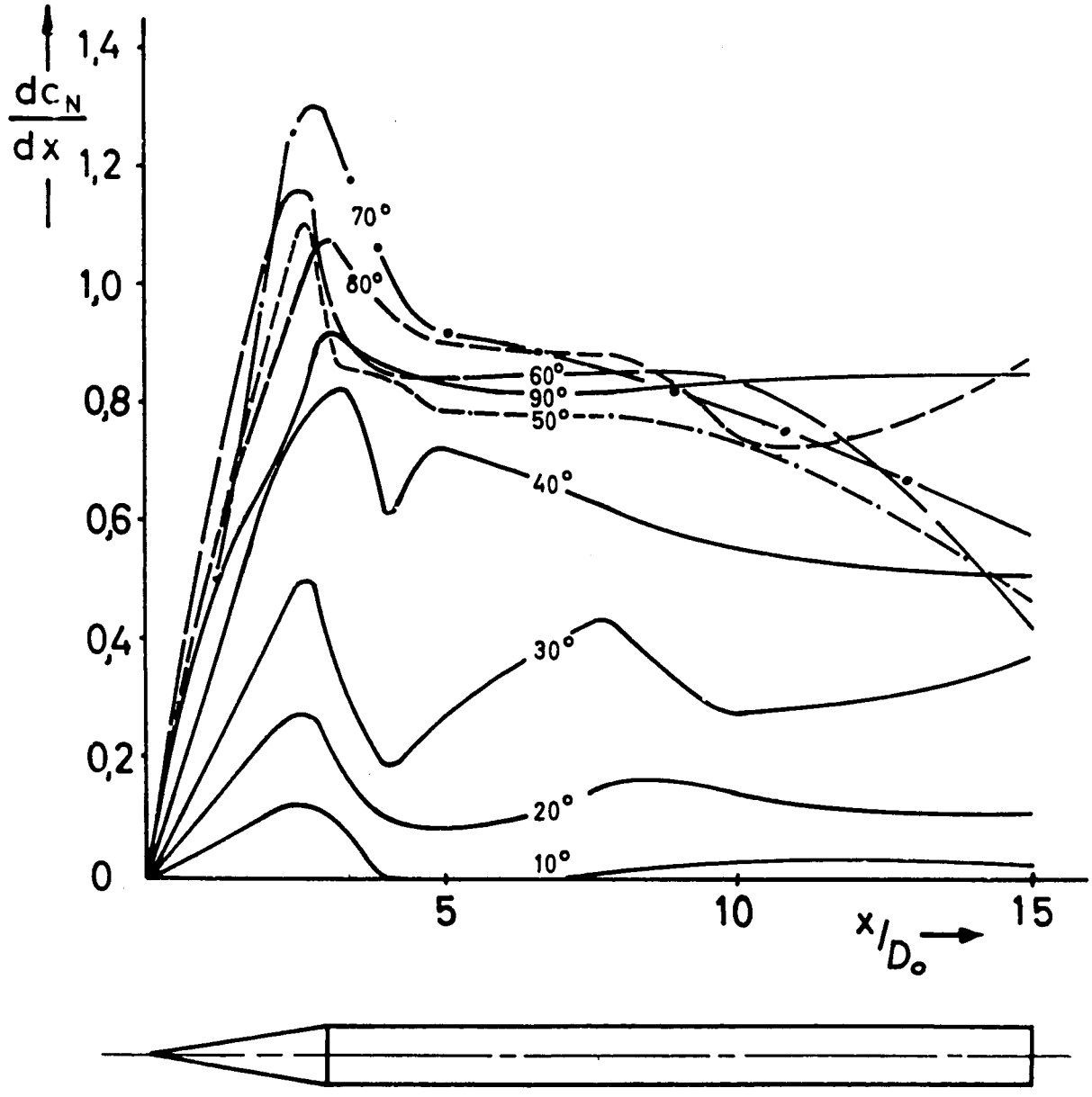

Fig. 19

Normal force distribution for body with cone-shaped head

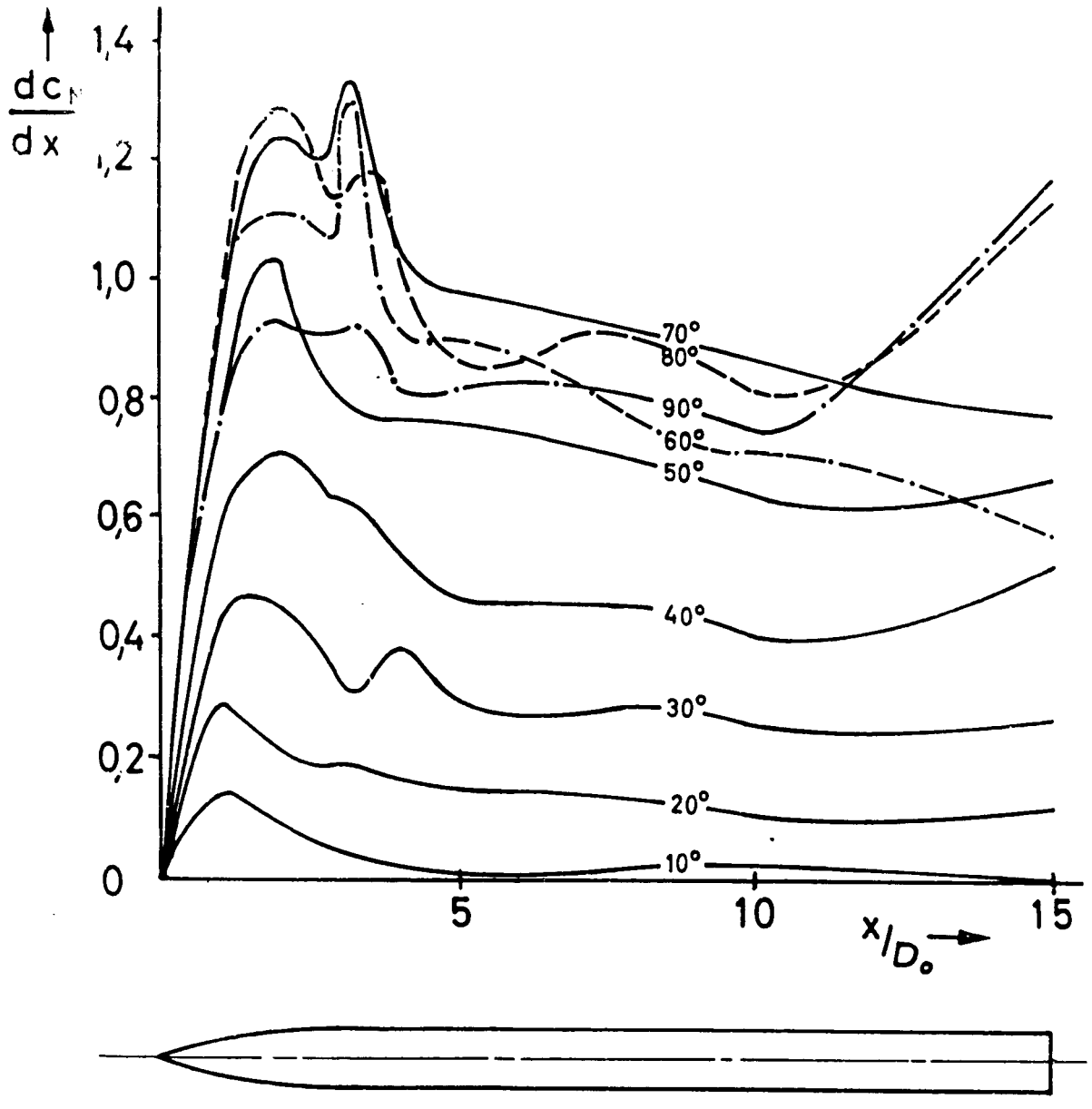

Fig. 20

Normal force distribution for body with ogivalic head

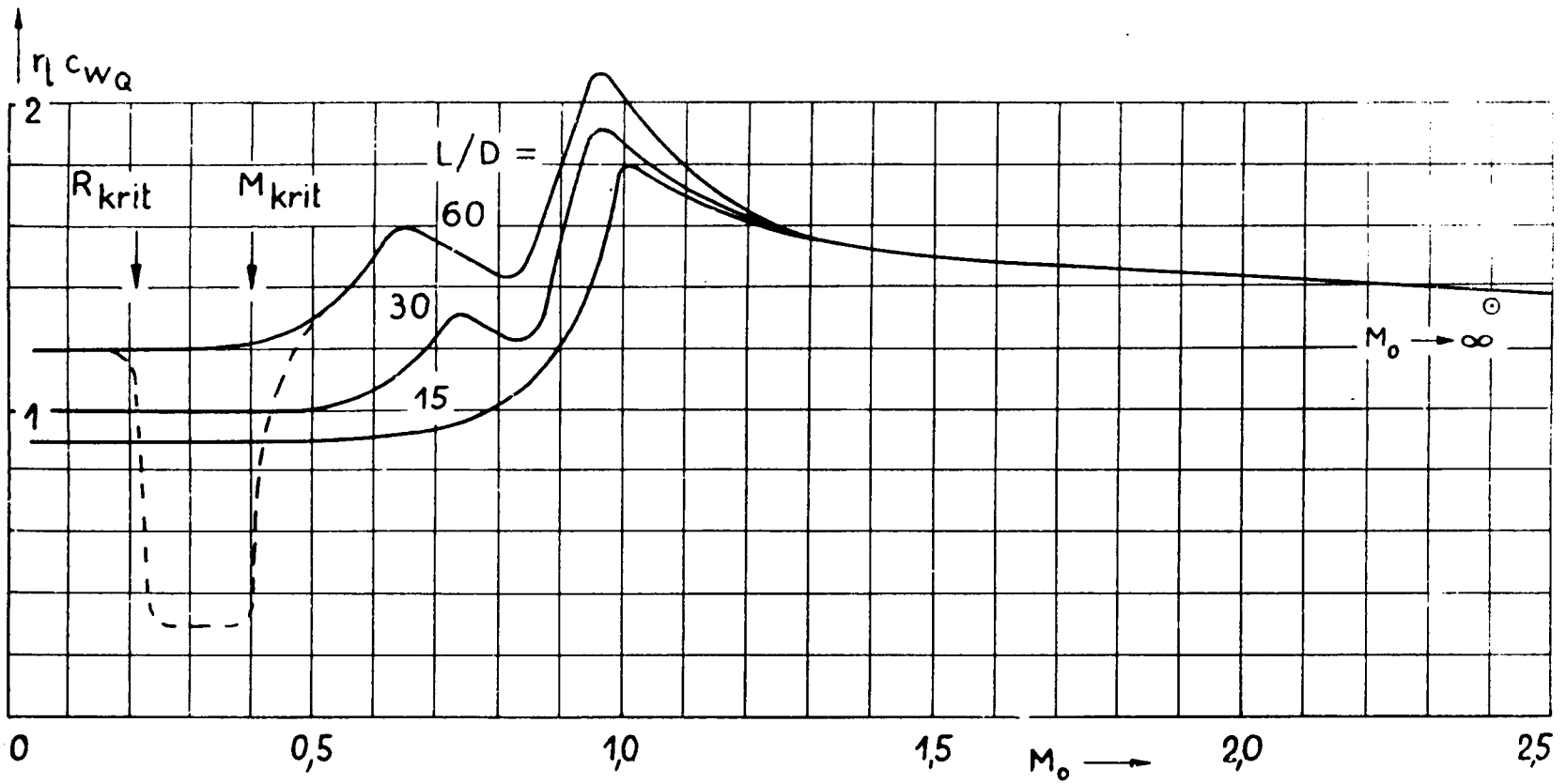

Fig. 21

Resistance coefficient per longitudinal cross-sectional area of laterally incoming current flow to circular cylinders of various lengths as a function of Mach number according to GOWEN and PERKINS [17]

$c_{N(\alpha=90°)} = \eta c_{WO}$

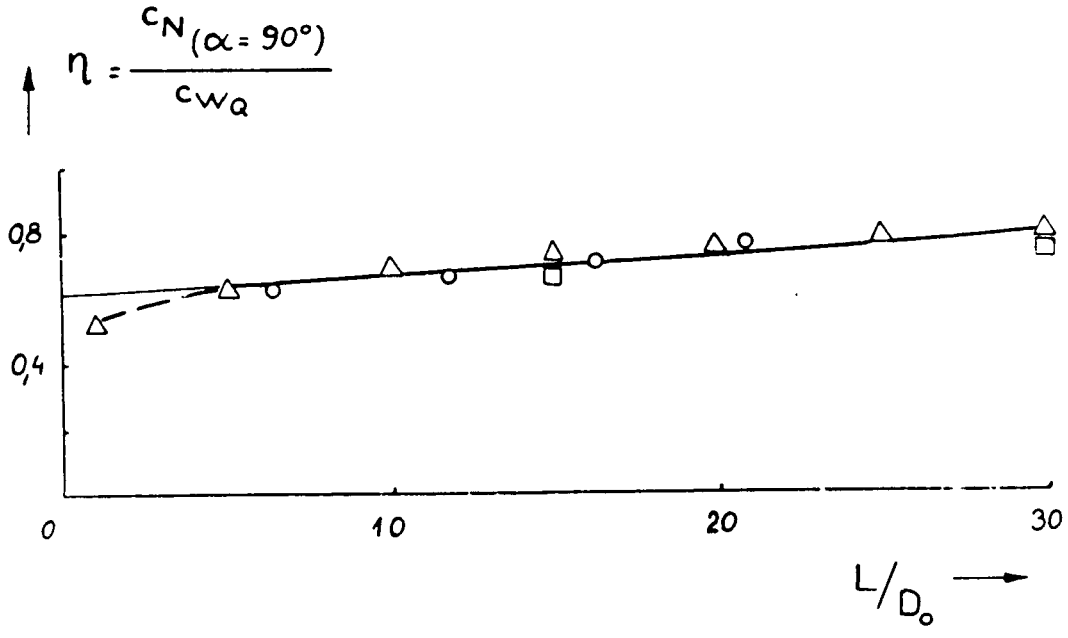

Fig. 22

Length influence factor η as a function of cylinder length at subcritical Mach- and Reynolds numbers according to [17]

_____ Equation (15)

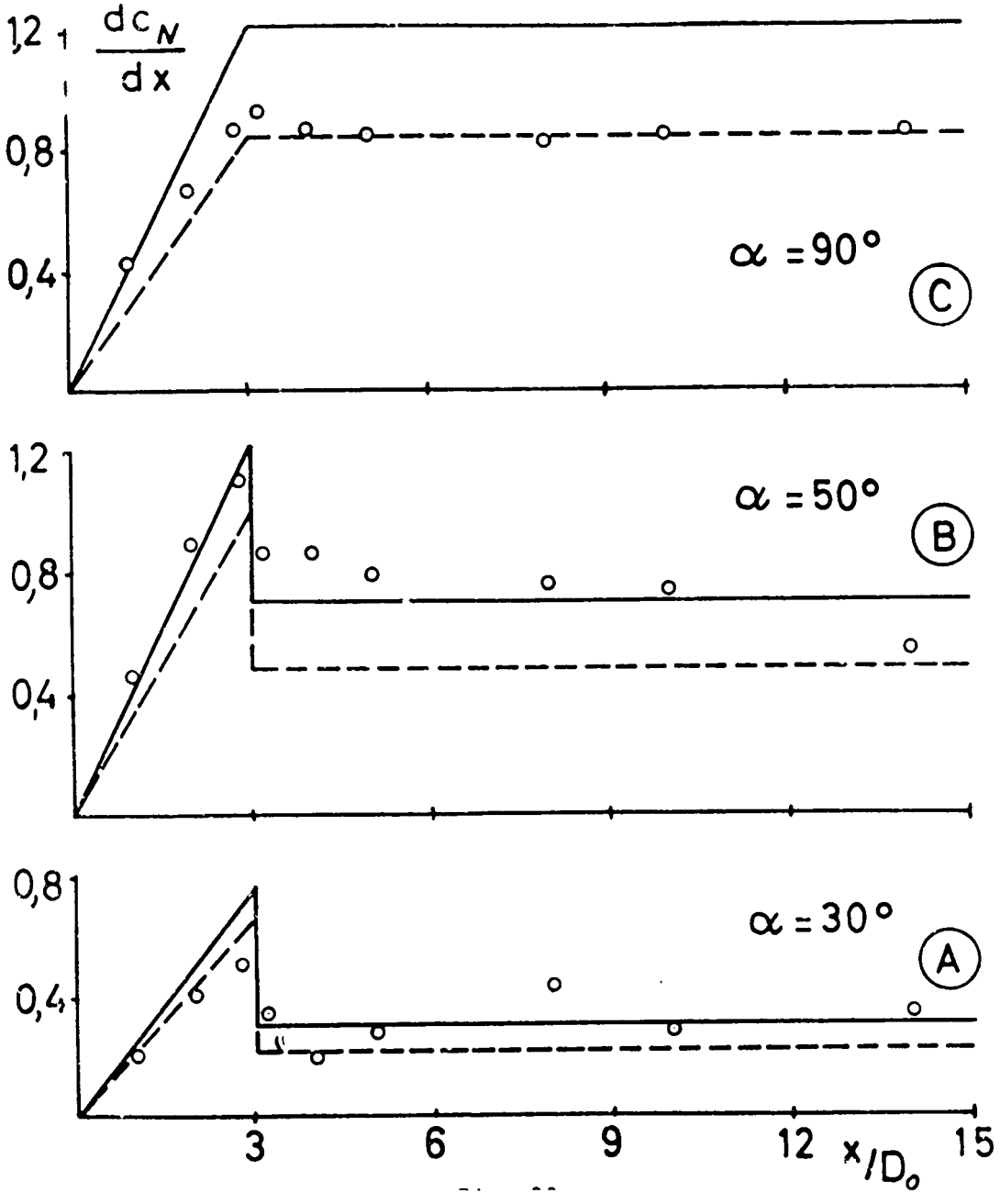

Fig. 23

Experimental and theoretical normal force distribution above the body axis for the body with the cone-shaped head, for angles of incidence 30° (A), 50° (B), 90° (C)

_ _ _ _ _ Equation (14)

_____ Equation (14) with $\eta = 1$

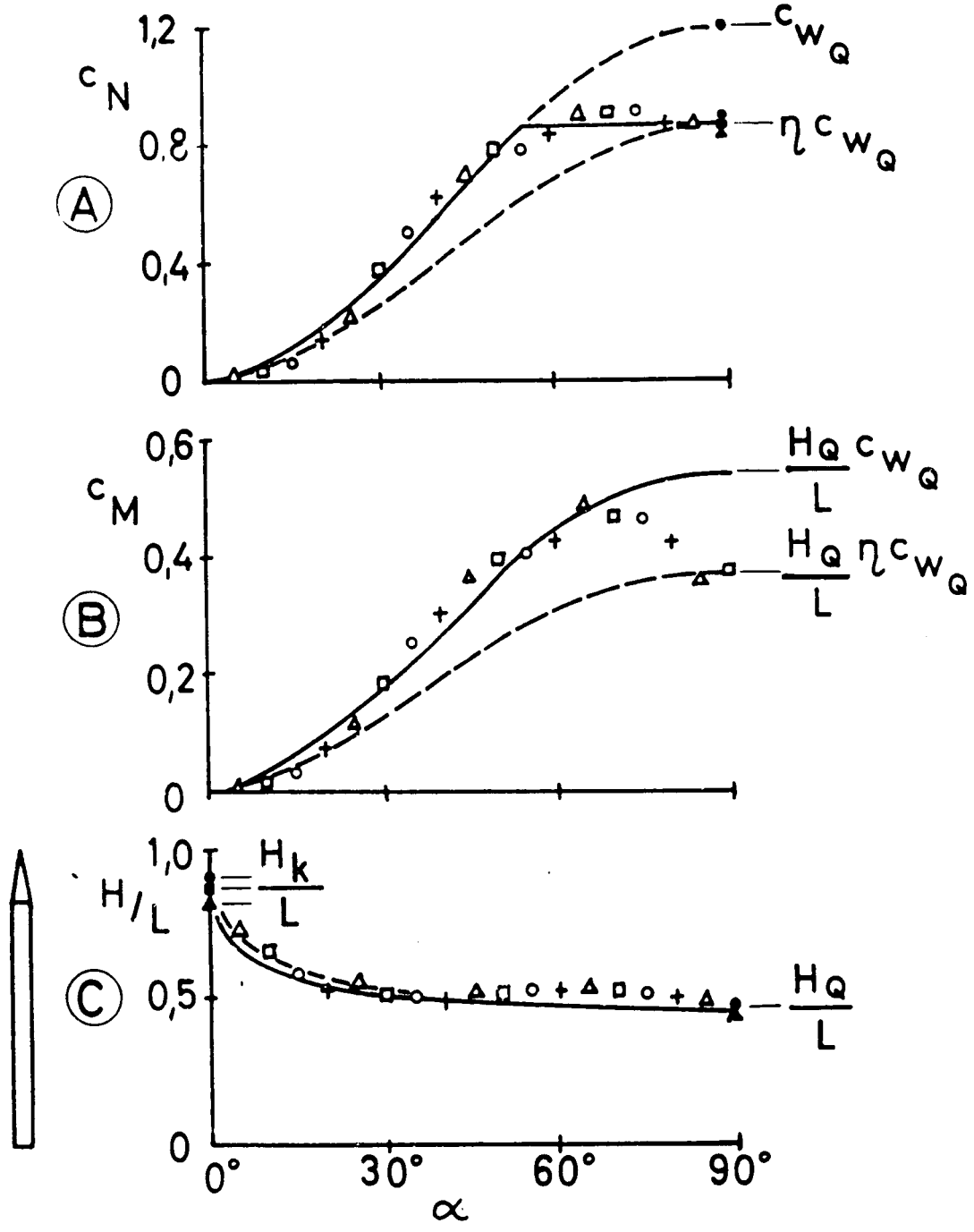

Fig. 24

Experimental and theoretical values for body with cone-shaped head,

(A) normal force coefficients

(B) coefficients of moments around the tail

(C) distance of center of pressure from tail

_ _ _ _ _ Equations (16) (17)

_____ Equations (16) (17) with n = 1

force measurements with the body lengths L/D_0 = 11.7 o

" " 16.3 □

" " 20.9 Δ

from the pressure distribution measurements 15.0 +

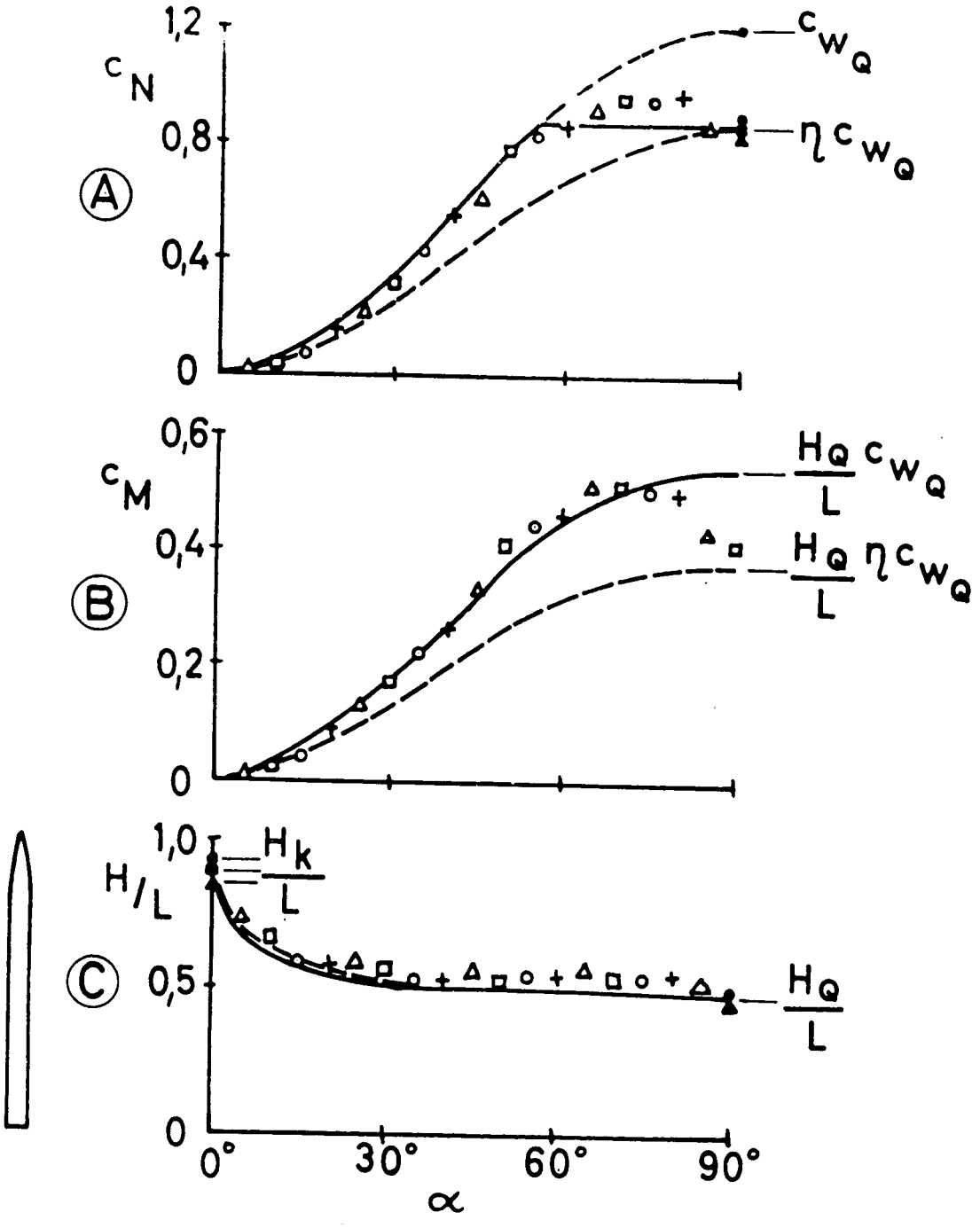

Fig. 25

Same as Fig. 24, but for body with ogivalic head

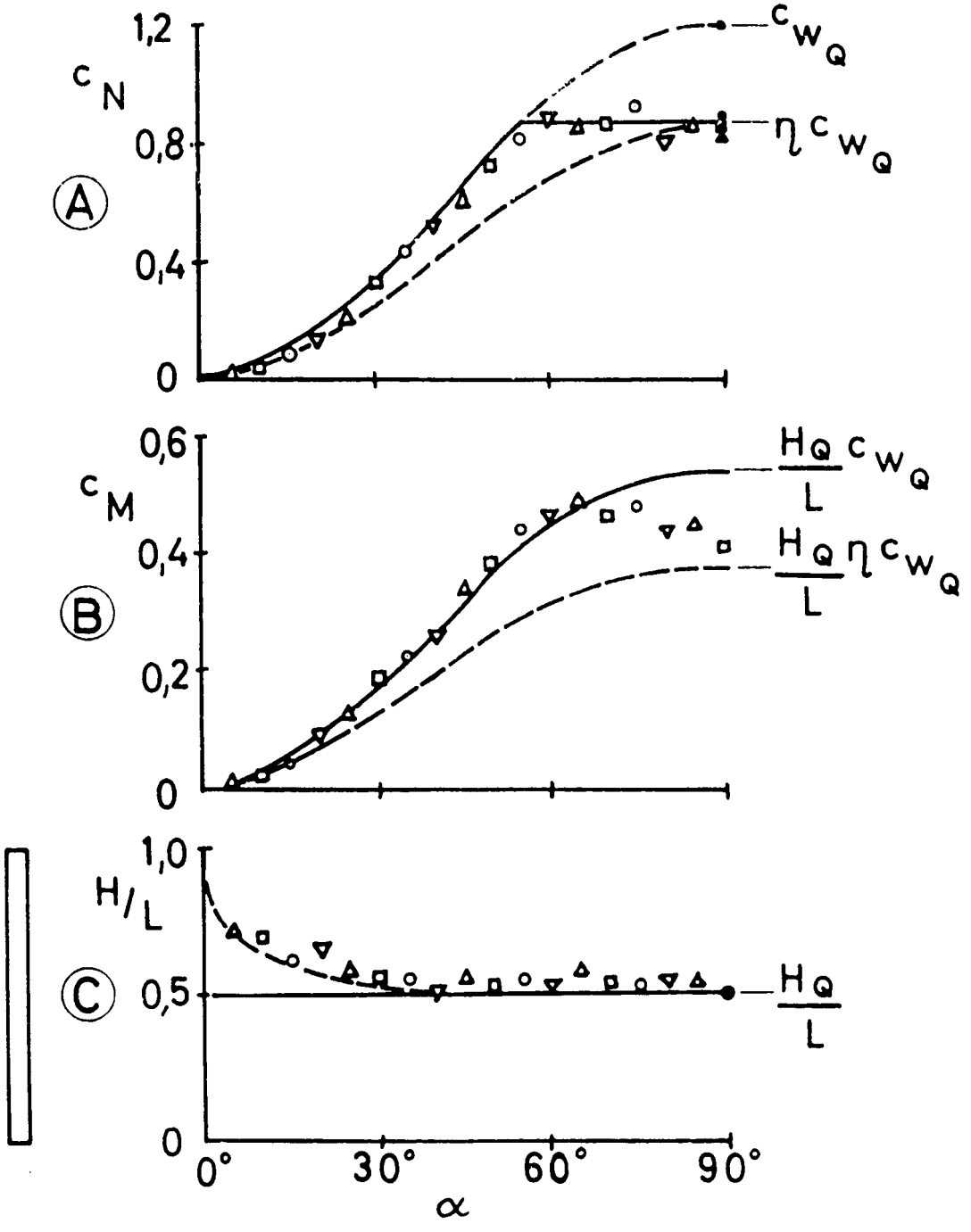

Fig. 26

Like Fig. 24, but for a straight-cut circular cylinder, graphs from Fig. 25, symbols like Fig. 24, but add $L/D_0 = 6.4$ ▽

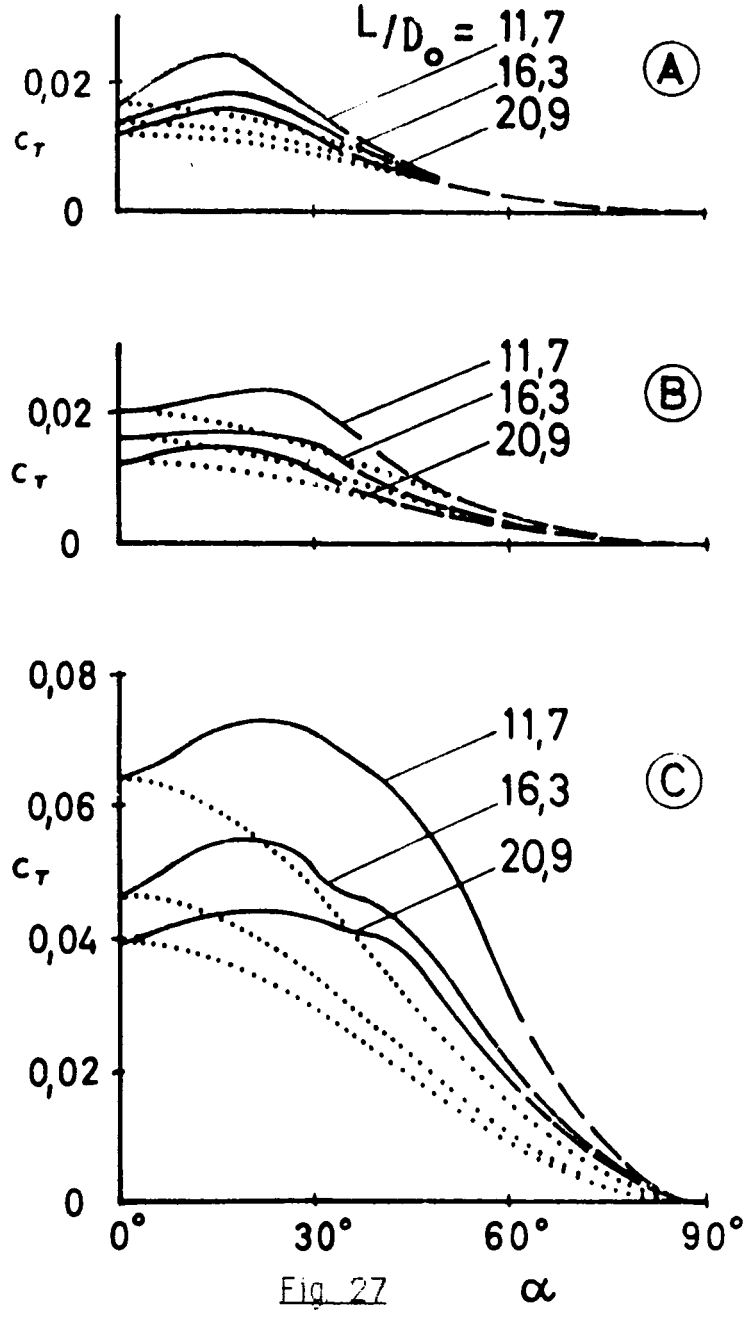

Fig. 27

Tangential force coefficients for circular cylinder

(A) with ogivalic head

(B) with cone-shaped head

(C) straight-cut

———— measured

– – – – – – presumed path of graph

..... $c_T = c_{T0} \cos^2$ å, Equation (18)